Physics of Fluids

Active control of vortex shedding past finite cylinders under the effect of a free surface

Cite as: Phys. Fluids **35**, 045130 (2023); https://doi.org/10.1063/5.0147760
Submitted: 25 February 2023 • Accepted: 30 March 2023 • Published Online: 13 April 2023

I. A. Carvalho and G. R. S. Assi

Physics of Fluids ARTICLE scitation.org/journal/phf

Active control of vortex shedding past finite cylinders under the effect of a free surface

Cite as: Phys. Fluids **35**, 045130 (2023); doi: 10.1063/5.0147760
Submitted: 25 February 2023 · Accepted: 30 March 2023 ·
Published Online: 13 April 2023

I. A. Carvalho[1,a] and G. R. S. Assi[2,b]

AFFILIATIONS

[1]Department of Mechanical Engineering, EPUSP, University of São Paulo, São Paulo, SP 05508-030, Brazil
[2]Department of Naval Architecture and Ocean Engineering, EPUSP, University of São Paulo, São Paulo, SP 05508-030, Brazil

[a]Author to whom correspondence should be addressed: amorim.icaro@usp.br
[b]Electronic mail: g.assi@usp.br

ABSTRACT

This paper presents the analysis of the active flow control promoted by low-aspect-ratio cylinders under the effect of a free surface at a low Froude number, modeled as a slip-allowing plane. To advance the literature in this merit, that is scarce compared with infinitely long and surface-mounted bodies, we carry out Detached-eddy simulations at Reynolds number of 1000 to investigate the active control provided by eight spinning rods surrounding a larger body. One of the ends of this system was immersed in the free stream, while the other was in contact with a free water surface. Our results reveal that when the rods spun with sufficiently large angular velocities, the (non-Kármán) vortex street was progressively organized and the part of the wake associated with the mechanism of vortex formation described by Gerrard ["The mechanics of the formation region of vortices behind bluff bodies," J. Fluid Mech. **25**, 401–413 (1966)] was eliminated. Nevertheless, tip-vortices prevailed throughout the examined range of spinning velocities. We also contrasted drag mitigation with power loss due to viscous traction and found that to reduce the mean drag on the system to a lower value than that of the bare cylinder necessarily required power expenditure. Steady reduction of mean drag and less significant mitigation of root mean square of lift and mean side force were verified to occur for the entire system and for the central body. However, the side force proved less affected by the wake-control mechanism. We demonstrate this to be associated with a novel ring-like vortex that prevailed throughout the simulations. Vortex dynamics and formation of these turbulent structures are explored.

I. INTRODUCTION

It is known that the greater the obstruction a body ("bluffness") causes to the incoming flow, the more likely it is that as the flow attempts to travel about the body, separation will occur due to the formation of a negative pressure gradient. In such cases, the boundary layer detaches from either side of the body in the form of shear layers. For cylinders, the communicating shear layers, with opposite vorticity, roll up and interact in the form of vortices, in a fashion that they draw vorticity from one another, lose some of it to the wake, and are utterly dissipated as they travel downstream away from the structure due to viscous effects (Gerrard, 1966).

Bluff bodies are prone to vortex-induced vibration (VIV), a phenomenon that causes these structures to obey a cyclic motion, both in the direction of the incoming flow and (more intensely) in the transverse direction (Williamson and Govardhan, 2004). Fatigue and failure due to VIV upon offshore structures are some of the undesirable occurrences that pushes forward interest to control the flow, to ultimately prevent or attenuate vibrations. Low-frequency and high-amplitude oscillations are found to occur to large oil rigs that possess an extensive, bluff hull, such as in spar and monocolumn platforms, particularly in activities of the offshore industry devoted to ultra deep water exploration. Within this context, vortex-induced motion (VIM, Gonçalves *et al.*, 2010) is a more common terminology for the fluid–structure interaction, where the amplitude of vibration scales with the characteristic length of the body (Fujarra *et al.*, 2012). Contrarily, for the hydrodynamic power generation, it is often of interest to provide conditions for the motion with non-null, but controlled amplitude. A stepping stone toward VIV suppression or its build-up lies in understanding and controlling vortex dynamics. Thus, vortex-shedding control is a relevant path toward flow control that may directly impact structures subject to vibration.

To achieve flow control, passive technologies have been proposed in the literature (Zdravkovich, 1981). This category comprises shrouds

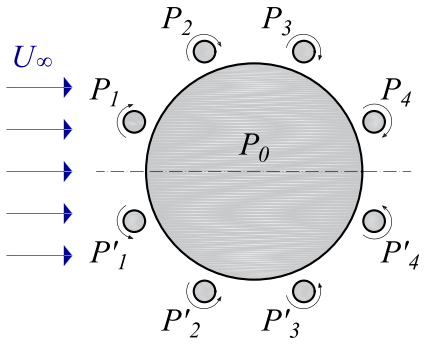

FIG. 1. A cross section of the geometry. The incoming flow at velocity U_∞ reaches the entire system, comprised of the main body denoted P_0, and upper and lower slender rods, respectively, denoted P_n and P'_n, for $n = 1, \ldots, 4$. Frontal rods P_1, P'_1 and rear rods P_4, P'_4 are displaced from stagnation regions by 22.5°. All rods are uniformly distributed about the main body. The figure is not to scale for better visualization.

(Cicolin and Assi, 2017), near-wake stabilizers (Strykowski and Sreenivasan, 1990), and surface protrusions, such as splitter plates and free-to-rotate fairings (Assi *et al.*, 2009; Assi *et al.*, 2014), but the most known are probably helical strakes employed in risers (Korkischko and Meneghini, 2011). These technologies have been vastly studied and have shown to work up to some Reynolds number $Re = U_\infty D/\nu$ (where U_∞ is the free-stream velocity, ν is the kinematic viscosity of the fluid, and D is the dimension of the body). For *Re*-values below 100, Strykowski and Sreenivasan (1990) showed that a slender rod, properly positioned near the main larger body, was suited to suppress global instabilities of the flow and, thus, precluded the onset of vortex shedding entirely. All of these technologies focused on the reattachment of the shear layers, reduction of their interaction or delayed entrainment of fluid further downstream, so as to dissipate the circulation of the communicating shear layers beforehand.

Active techniques require power input. In doing so, several works showed that technologies of this type have been more apt to control the wake and vortex shedding at higher *Re*-regimes (Choi *et al.*, 2008). One form that has called attention is that using spinning rods, based on the moving surface boundary-layer control (MSBC), originally from the aerodynamics context. In MSBC, momentum is injected into the near flow to delay separation. To provide the spinning elements with increasingly higher angular velocities proved effective to reduce mean drag and the fluctuating lift and eliminate vortex shedding entirely (Mittal, 2001).

Beyond these results, a configuration where the main and larger body of diameter D is fitted with eight slender rods of diameter d, distant from the main body by a gap G, as shown in Figs. 1 and 2(a) was employed by Assi *et al.* (2019). In such a setup, the active mechanism is characterized by the rotation of the wake-control rods about their own axis. The authors showed that to provide these spinning rods with sufficient actuating power gave rise not only to the results attained by Mittal (2001) with one rod, but extended to produce thrust upon the entire system. Thus, the rotating mechanism promoted a mean drag inversion and released greater flow control than its passive counterpart and the rotating mechanism with fewer spinning elements. Ongoing studies have shown that this system with eight rods behaves omnidirectionally relative to changes in the angle of attack of the incoming flow (Carvalho and Assi, 2023a; Carvalho and Assi, 2023b), in the sense that the same level of wake control and load attenuation were found at different angles of attack of the incoming flow in laminar and turbulent regimes of infinitely long bodies (Carvalho and Assi, 2023a; Carvalho and Assi, 2023b, with an active mechanism as described in Sec. III B), an important feature in considering technological applications, wherein the incoming flow direction might not be aligned with the centerline of the entire system, and the flow control should be desirable.

This technology was found to work with an equivalent system but free to develop VIV (Silva-Ortega and Assi, 2017b), and other arrangements have also been explored with different numbers and locations of the rods (Silva-Ortega and Assi, 2018). However, the configuration with eight rods was less susceptible to the increase in hydrodynamic loads and to galloping.

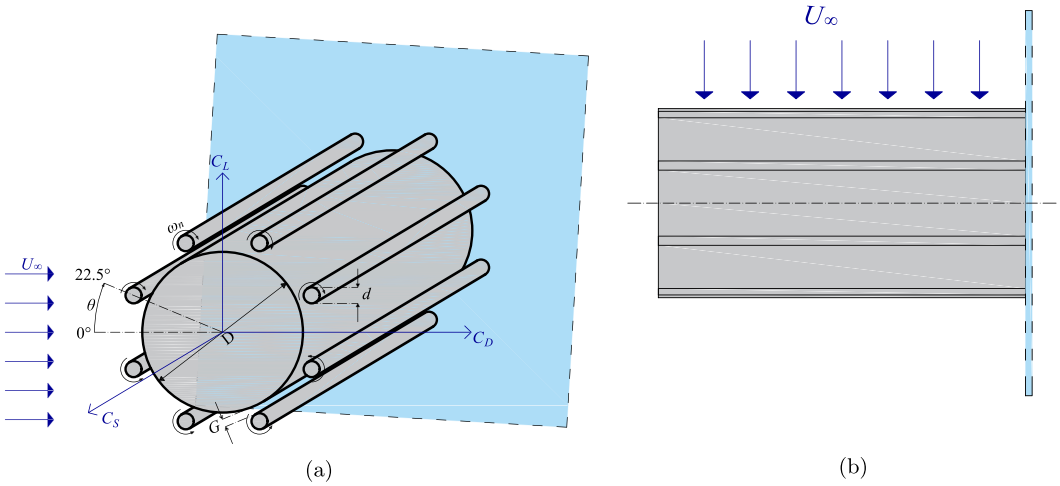

FIG. 2. Geometrical parameters of the entire setup: length (L), gap (G), rods' diameter (d), main body diameter (D), and angle coordinate (θ). Hydrodynamic loads: lift (C_L), drag (C_D), and side forces (C_S). The incoming flow is aligned with the x-direction. Figures are not to scale.

Notably, most of previous works have been concerned with infinitely long bodies, where end effects were disregarded, despite the paramount work of Williamson (1996), where the author explicated the relevance of the ends of the body to the three-dimensionality of the flow and to vortex dynamics phenomena, even for long aspect ratio bodies. However, little is found in the literature regarding flow control over these structures. As a matter of fact, as reported by Rosetti *et al.* (2013), a general lack of studies is found for the flow over low aspect ratio bodies (without wake control). Studies with a wake-control device for systems under the effect of a free water surface are even scarcer.

Generally, published works examined the flow over surface-mounted bodies (Sumner, 2013; Gonçalves *et al.*, 2015). Farivar (1981) studied the subcritical flow over a fixed plain cylinder (one without a wake control device) with aspect ratios between 2.78 and 12.5 at $Re = 7 \times 10^4$. The author found that in terms of hydrodynamic loads, the mean effect produced by the ends was in the decrease in the mean drag coefficient (previously noted by Kawamura *et al.*, 1984) as the slenderness parameter (given by the ratio of the length by the diameter of the cylinder, L/D) decreased. Later, this observation was supported by experiments at very low aspect ratio (Gonçalves *et al.*, 2015) and numerical simulations (Palau-Salvador *et al.*, 2010, showed that, through wake topology visualization, this is to be related to downwash vortex formation).

In the scope of a free water surface as the work we propose here, Gonçalves *et al.* (2015) assessed slenderness parameters between 0.1 and 2.0 and observed that monocolumn and spar platforms as well as semi-submersible columns fit into this range. The paper also rendered clear that notwithstanding similarities exist between wall-mounted and free-surface configurations, these setups present flow features of their own due to the different boundary conditions. For example, in free-surface configurations, the cylinder is not immersed in a boundary layer.

We further remark that in spite of these studies, flow control in the form of interference with slender rods is still a field to be unveiled when it comes to finite bodies. As mentioned in Carvalho and Assi (2023c), although the study of Luo *et al.* (1996) assessed the interaction between two low aspect ratio cylinders of sizes of the same order of magnitude, such study was not dedicated to flow control.

As it can be seen, although the problem of the flow past finite cylinders has been investigated, chiefly for the wall-mounted and large aspect ratio setups; in general, flow control of low aspect ratio bodies with a free surface remains vastly unexplored.

II. OBJECTIVE

We intend to advance the current state of information by bringing the MSBC technology, implemented in the form of spinning rods, to comprise an active mechanism of flow control for finite cylinders with a free surface, modeled here a slip-allowing plane. The system is represented in Fig. 2. Some of the matters addressed in this work are (1) the extent of realizable flow control by this active mechanism against end effects and tip-vortex and their suppression; (2) the efficiency of the entire system, assessed through the conflicting goals of mean drag decrease and economical spinning setups; and (3) vortex dynamics interplay and consequent effects upon the structure.

The results from the numerical simulations performed at $Re = 1000$ will be investigated in terms of hydrodynamic loads, wake topology, wake interaction with the free surface, and free-end effects. We compare passive (as in Carvalho and Assi, 2023c) and progressively more power-demanding active mechanisms to one another, as well as with the reference case of a bare cylinder (without wake-control rods).

The present study constitutes part of a research effort to devise suppressing devices to mitigate VIV of floating offshore structures. Knowledge of the physical mechanisms acquired from numerical simulations should help the development of active and passive technologies to control the flow about bluff bodies.

III. METHOD

A. Problem description

We investigate the setup of Fig. 2 (three-dimensional visualization of Fig. 1). An incoming flow U_∞ reaches the arrangement comprised of a main body P_0 of diameter D fitted with an active-control device. The control mechanism is exerted through $N = 8$ slender rods of diameter $d = D/20$ that spin about their respective axes with angular velocities ω_n to inject momentum into the outer flow about the entire system. These rods are distant from the wall of the main body by the gap $G = D/100$. Upper rods $P_1, \ldots, P_4$ spin clockwise with the same magnitude, but opposite direction to that of the lower rods $P'_1, \ldots, P'_4$, so that $\omega_n = -\omega'_n$, $n = 1, \ldots, 4$. Wake-control rods are deliberately positioned away from the stagnation regions by 22.5° and uniformly distributed, so consecutive rods are separated by a 45° angle. The same configuration, but restricted to a passive analysis, was employed earlier in the literature (Carvalho and Assi, 2023c). We emphasize that all cylinders are modeled as finite bodies of low aspect ratio, with length $L = 2D$; thus, end effects are considered. See Fig. 2(a) for the representation of these geometrical parameters. As exhibited by Fig. 2(b), on one end of the entire system is located a free water surface, modeled here an infinitely long slip-allowing plane; and the other end is within the free stream.

This setup was chosen based on previously published results and ongoing work. Silva-Ortega and Assi (2017a) compared different numbers of rods, diameters, and gaps and found that $N = 8$ rods were capable of attenuating VIV amplitude by 99% with $G/D = 0.1$. We used $d/D = 0.1$ (instead of $d/D = 0.08$, as in Silva-Ortega and Assi, 2017a), following Assi *et al.* (2019). For this parameter, it suffices that the rods should be sufficiently small to interact with the shear layers of the larger body. Furthermore, as reviewed in Sec. I, this system has shown an omnidirectional attribute, provided that the angular velocities are defined as in Sec. III B.

Finally, regarding possible wave interactions on a real free surface, we verified that the Froude number based on the cylinder's length (given by $Fr = U_\infty/\sqrt{gL}$, where g is the gravitational acceleration) was inferior to 0.23. According to Newman (2018), for a subcritical regime of $Fr < 1$, the wave pattern is similar to that expected for deep waters. Generally, for $Fr < 0.5$, water elevation due to free surface effects is deemed negligible. Thus, since wave effects are not significant in the present study, our setup fits well in these conditions and the free surface can be adequately represented by a slip-allowing plane. Gonçalves *et al.* (2018), for example, employed a similar approach for an experimental investigation of floating bluff bodies in a water channel.

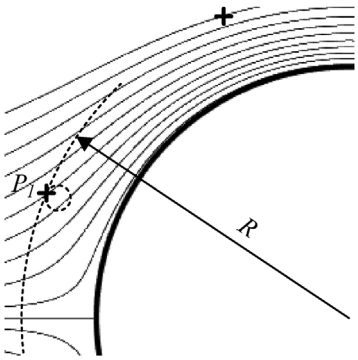

FIG. 3. Potential flow about a bare cylinder. Within this flow configuration, streamwise velocities were computed at polar positions corresponding to the outmost point that will be located on the surface of the rods relative to the center of the entire system in the viscous flow.

B. Definition of rotation rates

The angular velocities imposed to the rods are obtained from a potential-flow analogy, as in previous works (Carvalho *et al.*, 2021; Carvalho and Assi, 2022, although in the context of infinitely long bodies). For this derivation, we consider the polar coordinates $\theta = \pm 22.5 \pm 45°(n-1)$ and $R = D/2 + G + d$ that mark the farthest point located on the surface of the rods relative to the center of the entire system (see Fig. 3 for an example). At these points, streamwise velocity components V_1, V_1', …, V_4, V_4' are calculated from the potential flow about a bare cylinder, as depicted in Fig. 4.

The analytical expression of V_n in the potential flow is given by the following equation:

$$V_n = U_\infty \left\{ \hat{r}[\cos(\theta_n)] \left[1 - \frac{(D/2)^2}{(D/2+G+d)^2} \right] + \hat{\theta}[-\sin(\theta_n)] \left[1 + \frac{(D/2)^2}{(D/2+G+d)^2} \right] \right\} \cdot \hat{\theta}, \quad (1)$$

(for $\zeta = 1.0$, see Carvalho *et al.*, 2021). These same velocities are then imposed in the viscous flow about the entire system, to the control rods in the form of angular velocities $\omega_n = V_n/(d/2)$. To modify these rotation rates proportionally, the parameter ζ was employed so that $\omega_n = \zeta V_n/(d/2)$ for $\zeta = 0.0$ (passive rods), 0.5, 1.0, 2.5, and 3.5.

C. Numerical scheme

The numerical scheme employed in this work is analogous to Carvalho and Assi (2023c). The Navier–Stokes and mass conservation equations, representative of the incompressible flow of a Newtonian fluid,

$$\rho\left(\frac{\partial U_i}{\partial t} + U_j\frac{\partial U_i}{\partial x_j}\right) = -\frac{\partial p}{\partial x_i} + \mu\frac{\partial^2 U_i}{\partial x_j \partial x_j}, \quad (2)$$

$$\frac{\partial U_j}{\partial x_j} = 0, \quad (3)$$

(given in a differential form) were solved through a finite-volume discretization that is described below. In Eq. (3), ρ refers to the fluid density, $\mathbf{U}$ and $\mathbf{x}$ are the velocity field and stations of the flow domain with components indexed by i and j (U_i, U_j, and x_i, x_j), $p = p(\mathbf{x})$ denotes the pressure field, and μ is the dynamic viscosity. We have solved this flow in the open-source C++ library OpenFOAM at a Reynolds number $Re = U_\infty D/\nu = 10^3$ based on the main cylinder's diameter D. We note that this nondimensional based on the rods' diameter is given by $Re_d = U_\infty d/\nu = 50$, at the onset of vortex shedding. Because the rods rotate, and this has shown to interfere with vortex shedding (Mittal and Kumar, 2003), we consider a priori that elements will not produce vortex shedding, thus will not interfere with that sourced from the larger body. This will be confirmed *a posteriori* in Sec. IV.

In order to ensure quality results, all terms hereby discretized followed second-order accuracy interpolants. An implicit backward scheme was employed for the transient term $\partial U_i/\partial t$ of the left-hand side of Eq. (3), while for the Lagrangian convective term $U_j\partial U_i/\partial x_j$, a blend of the linear upwind and central scheme was employed (based 25% on the former, and 75% on the latter), called LUST in the aforementioned library. Least squares were used to calculate gradients. Because our numerical scheme is cell-centered, interpolation of values to the surface of the cells was carried out with linear interpolation. Both structured and unstructured regions contained elements whose centers were not aligned perpendicularly relative to the interface between them; thus, it was necessary to impart a non-orthogonality correction to the surface normal gradient (along with the Gauss theorem). This procedure also allowed computation of the Laplacian term.

A known issue in the numerical solution of incompressible flows is the uncoupled variables velocity and pressure. In fact, Eqs. (2) and (3) rely only on the pressure gradient rather than on the pressure itself;

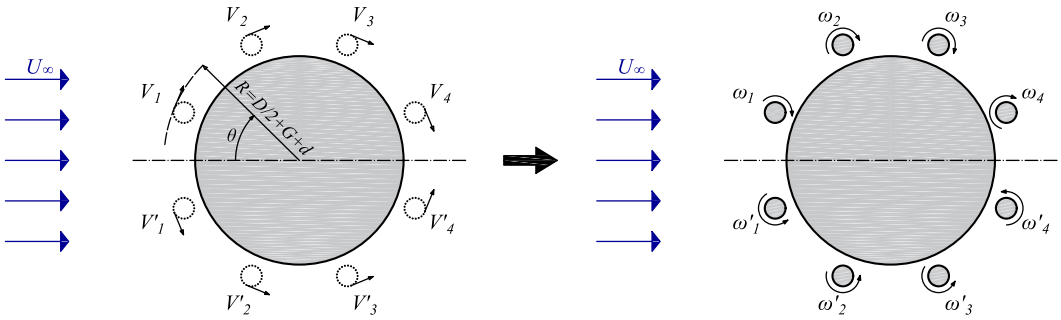

FIG. 4. Velocity vectors computed from the potential-flow field at points located in radial coordinates $R = D/2 + G + d$. $\theta = \pm 22.5° \pm (n-1)45°$, with $n = 1, \ldots, 4$ were assigned as equivalent angular velocities for the rods.

thus, these equations may be solved erroneously ignoring the pressure field itself, which is transported through the flow domain. To avoid this issue, these variables were solved together through the unsteady version of the semi-implicit method for pressure-linked equation (SIMPLE) coupling algorithm (Patankar, 1980).

In short, SIMPLE revolves about guessing the pressure field and solving Eqs. (2) and (3) together for the velocity (and turbulence modeling for further variables), where a correction term is found, that is then reapplied in the solution procedure. One of the terms is dropped to ease the solution procedure that would zero in upon convergence. Details of this method are explored in Patankar (1980). Residue tolerances of 10^{-4} for the solution of the pressure and 10^{-8} for the velocity components and other scalars were required for convergence at each time step, with the further requirement of at least 10 outer loops at each time step. The work of Carvalho and Assi (2022) showed that this lower tolerance for the pressure did not compromise the results and yet allowed for faster run times.

Rhie and Chow's interpolation was used to prevent the so-called *checker-board effect*, whereby a third-order pressure term was included for the computation of face velocities (Rhie and Chow, 1983). Among the advantages of this procedure, storage was more efficient, and the second-order accuracy is ensured.

In order to avoid information loss from one time step to another, time step size restrictions were enforced based on the rotation rate of the rods and on the reference vortex shedding cycle of a bare cylinder. Thus, time steps were limited from above by 1/70 of the revolution of the rods and by 1/100 of the timespan of a shedding cycle.

A linear system was obtained after discretization of all terms. After the solution of the linear system, the resultant forces were obtained through integration of viscous effects and pressure distribution over the surface of each body, and the components thereof, lift (F_L), side force (F_S), and drag (F_D), were obtained. Normalization was made by $1/2\rho U_\infty^2 DL$ to get the lift, side force, and drag coefficients C_L, C_S, and C_D, illustrated in Fig. 2.

General details of the finite volume formulation are found in Ferziger *et al.* (2002) and Versteeg and Malalasekera (2007).

D. Boundary conditions and meshing

Symmetry boundary conditions (no flow across) were imposed on the sides of the domain and on the free surface. The walls of the rods adopted the rotation rates explained in Sec. III B for $\zeta \neq 0$, and the no-slip condition was applied to their surfaces in the passive configuration of $\zeta = 0$. For the main body, the no-slip condition was ensured throughout simulations. The inflow was specified by a Dirichlet condition, the far-field flow of fixed velocity U_∞, and a Neumann condition corresponding to fully developed pressure gradient $\nabla p = 0$; conversely, the outflow was prescribed by a Neumann condition on the velocity and Dirichlet's for the pressure. The simplified geometry of the domain, together with the indication of inlet and outlet patches, is given in Fig. 5, in which L_S represents the distance from the system free end to the side of the domain.

From the free end to the farthest side of the numerical domain, an adequate distance $L_S/D = 8$ was imposed to avoid blockage effects. The center of the main cylinder was distant $8D$ from the top and bottom surfaces and from the inlet. A greater distance of $20D$ was applied between the main cylinder's center and the outlet downstream. These dimensions for the grid geometry corroborate with the work of Behr *et al.* (1995), Behr *et al.* (1991), Kim and Mohan (2005), and Carvalho and Assi (2022) for infinitely long bodies. A wider domain was investigated in the latter reference, and no significant changes were observed. In Carvalho and Assi (2023c), this same, but passive, setup was analyzed with the same meshing, and sufficiently accurate results were attained.

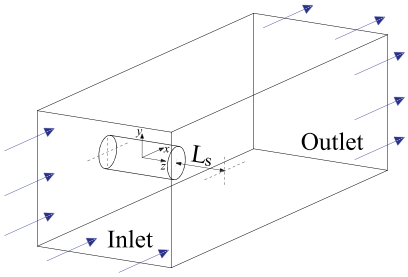

FIG. 5. Simplified geometry of the numerical domain. For clarity, the rods were not represented. As shown, the system is attached to the free water surface at $z = -D$ on one end and its other end, at $z = +D$ is free interacting with the free flow. Sides of the domain correspond to symmetry planes. The origin of the set of axes is placed at the center of the entire system.

Hexahedral and prismatic elements covered the flow domain, and the mesh was the more refined the nearer it was to the bodies or to the wake region, to capture typical gradients of the flow directly associated with vortices and eddies. Away from the cylinders and from the wake are located regions where gradients typically approach null value, and the flow asymptotically assumes fixed and fully developed boundary conditions. Toward these gradient-free locations, the cells were enlarged. Expansion of the cells adopted ratios lower than 10% and 14% for the bare cylinder and system grids, respectively. Figure 6(a) portrays a cross section passing through the system.

Triangular-faced elements can be observed to comprise the part of the lateral surface of the main cylinder in Fig. 6(b). Extrusion of the cylinders is also depicted, as well as the refinement along the span toward the ends of the bodies. It should be noted that it is the extrusion of the sidewall of these cylinders, that contains triangular elements, that led to the need of unstructured, prismatic, cells away from the ends and into the free stream. Nevertheless, predominantly structured and hexahedral elements were used. Near the wall, this choice of element is appropriate because the boundary layer contains a strong velocity gradient transversely to the wall (although weak longitudinally). Cross-sectional and spanwise views of rod P_1 are shown in Figs. 7(a) and 7(b). The latter captures the end fixed to the free surface.

The smallest elements measured $1.54 \times 10^{-3} D$ on the wall of the main body and $3.77 \times 10^{-3} d$ on the wall of the wake-control rods to ensure quality results near the boundary layer and to dispense with wall functions. In total, 19 153 204 cells were employed, comprised 81% of hexahedral elements.

Mesh convergence study was carried out in Carvalho and Assi (2023c) and has shown that our grid was sufficiently refined. For conciseness, this study will not be repeated here.

E. Turbulence modeling

Since the flow about cylinders is laminar for $Re < 190$, our flow at $Re = 1000$ was well into turbulent regime and its behavior was

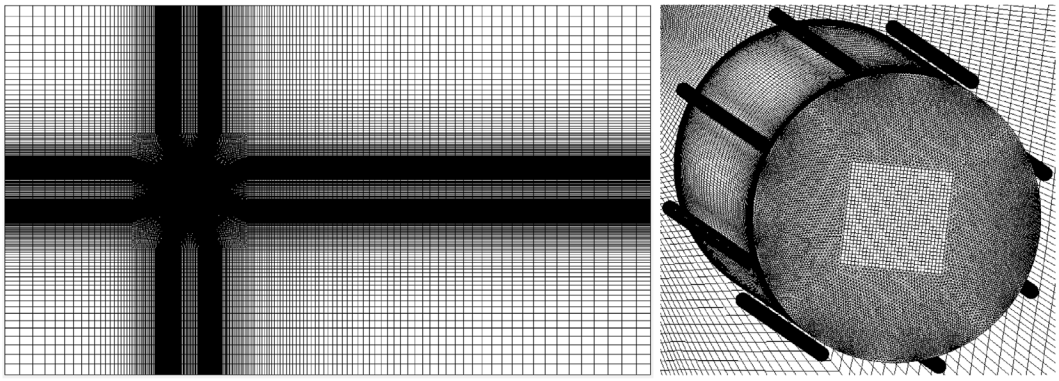

(a) (b)

FIG. 6. Different regions of the mesh. (a) Full domain and (b) side of the cylinders.

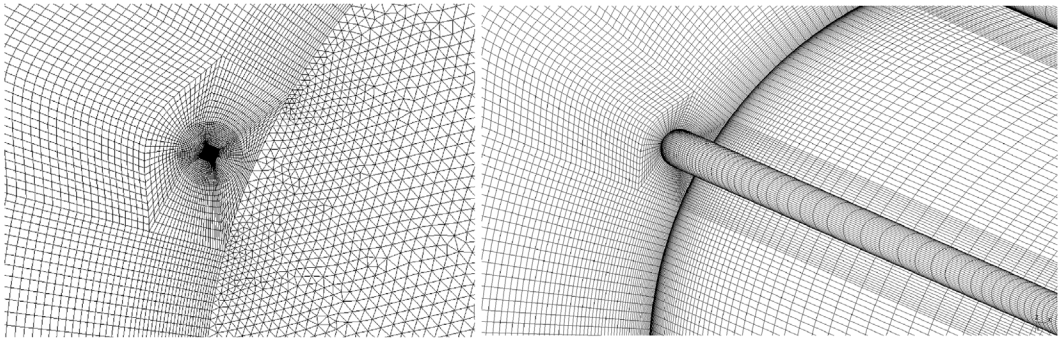

(a) (b)

FIG. 7. Close-in view of rod P_1. (a) Cross sectional view and (b) spanwise extruded view.

inherently three-dimensional (3D). Thus, we employed a 3D Detached-eddy simulation (DES, Spalart, 1997) so that large, detached, eddies were fully resolved, while the boundary layer was modeled by means of unsteady Reynolds-averaged Navier–Stokes (URANS) equations. Small, isotropic, and turbulent scales away from the boundary layer were modeled in agreement with the classical work of Smagorinsky (1963). The advantage of this procedure is that, in modeling only the small scales (that approximate better the turbulent universal behavior, Tennekes and Lumley, 1972), this approach has been proven to more computationally efficient (Spalart, 1997).

For the URANS part, we employed the one-equation model of Spalart and Allmaras (1992), which transports the turbulent viscosity parameter $\tilde{\nu}$ and relates it to the turbulent viscosity ν_t. This model has proven able to capture separation points adequately (Travin *et al.*, 2000). The appropriate boundary conditions in this case are those of Spalart (2000) and Vatsa *et al.* (2017),

$$\tilde{\nu}_{\text{wall}} = 0, \tag{4}$$

$$3 < \tilde{\nu}_{\infty}/\nu_{\infty} < 5. \tag{5}$$

For infinitely long and low aspect ratio cases, this approach was successfully verified against other numerical works and validated with experiments Carvalho and Assi (2022) and Carvalho and Assi (2023c).

Further consideration was required because in subcritical flow regime, the wake has transitioned to a turbulent state, whereas the boundary layer is still laminar. Therefore, a low-*Re* correction was necessary (Spalart *et al.*, 2006), because the URANS formulation is intrinsically turbulent and could interfere with the location of the separation points. We anticipate that this was prevented, and all simulations preserved a non-dimensional distance away from the walls of the cylinders $\mathcal{O}(y^+) \sim 1$, so we dispensed with wall functions.

The parameter $\tilde{\nu}$ followed a linear upwind scheme. Turbulence modeling parameters are exposed in Carvalho and Assi (2023c) and will not be repeated here for brevity.

IV. RESULTS

A. Time histories of hydrodynamic loads

Each simulation of the active mechanism was left to run for a timespan corresponding to 28 cycles of vortex shedding based on the flow about an infinitely long bare cylinder in subcritical regime that we shall henceforth denote T_S. For reference, we note that the Strouhal number is given by $S_t = 1/(T_S U_\infty/D) \approx 0.2$, where reasonable approximation is made based on several simulations and experiments (Norberg, 2001).

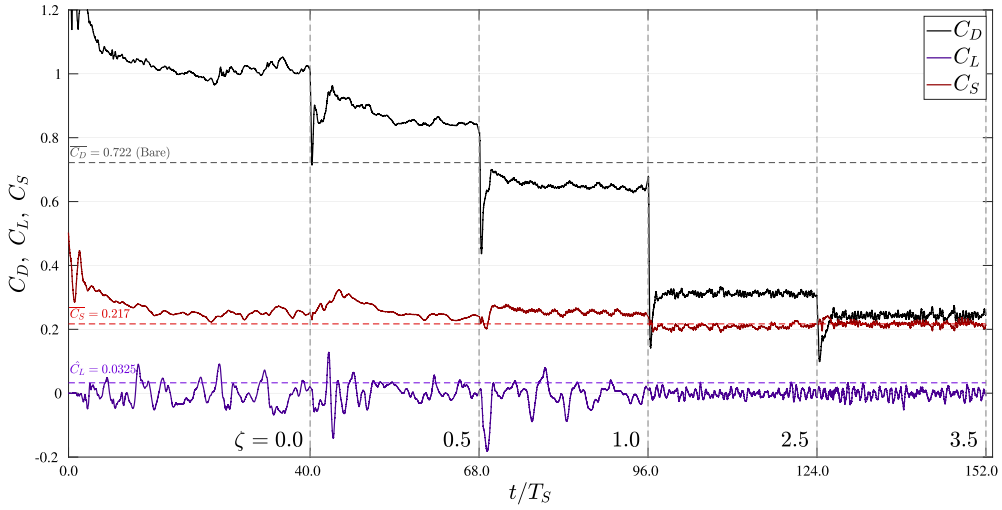

FIG. 8. Time histories of the drag (C_D), lift (C_L), and side force (C_S). Reference values of Eq. (6) for the bare cylinder are represented by dashed lines following the same color scheme.

For the passive setup, the last 25 cycles were assumed converged and, thus, considered for the computation of mean and root mean square (RMS) quantities, whereas for active setups, a timespan of 15 cycles were analogously assessed. The shorter number of cycles and run time of the setups involving spinning rods is justified because these simulations departed from the last time step of the passive setup. This procedure is known to provide faster convergence and was successfully employed in the literature (Mittal, 2001; Goodarzi and Dehkordi, 2017). From a physical standpoint, active setups faced much smoother loads, with lower fluctuation, as the time histories of Fig. 8 show. We anticipate that a simpler wake topology also resulted thereof.

The main trait verified previously from the usage of spinning wake-control rods, that of reduction of drag (C_D) and lift (C_L), is corroborated in Fig. 8. Increasingly higher rotation rates led to steady decrease in C_D. For C_L, perceptible attenuation was only verified for $\zeta \geq 2.5$, but neither a steady shrinkage of the amplitude nor complete elimination was observed as in Carvalho *et al.* (2021) or Carvalho and Assi (2022) for infinitely long bodies, where even its high frequency component faded away, given sufficient actuating power. This was expected for finite cylinders as the present, considering that the free-end is a geometrical singularity susceptible to separation due to its sharp corner. Interestingly, the side force (C_S) was virtually unaffected, except to some slight reduction for $\zeta \geq 2.5$ as in the amplitude of C_L, that might have to do with the increase in correlation of the wake that has been repeatedly shown to happen with sufficiently large rotation rates. These tendencies in the hydrodynamic coefficients of the entire system are quantitatively summarized in Table I. Percentages referring to changes from a ζ value to the passive setup render clear that the mean drag dropped consistently, while the other coefficients adopted an inconsistent trend.

From comparison of reference values of the bare cylinder expressed in Eq. (6) with those of Table I, it is interesting to note that to employ wake-control rods led mean drag ($\overline{C_D}$) and RMS of lift ($\hat{C}_L$) upon the entire system to lower values than those of the bare cylinder. In terms of mean side force ($\overline{C_S}$), the values of the entire system were comparable with $\overline{C_{S,\mathrm{Bare}}}$ in the affected regimes $\zeta \geq 2.5$; while for $\zeta < 2.5$, the rods caused $\overline{C_S}$ to be higher for the entire system,

TABLE I. Mean drag ($\overline{C_D}$), RMS of lift ($\hat{C}_L$), and side force ($\overline{C_S}$) coefficients. A steady trend of decrease in mean drag is observed, while $\hat{C}_L$ and $\overline{C_S}$ reduced only from $\zeta = 1.0$ to $\zeta = 2.5$. Percentages indicate change relative to the passive setup.

	Entire system		
ζ	$\overline{C_D}$	$\hat{C}_L$	$\overline{C_S}$
0.0	1.02 (-)	0.0358 (-)	0.252 (-)
0.5	0.873 (−14%)	0.0283 (−21%)	0.265 (+5.2%)
1.0	0.652 (−36%)	0.0368 (+2.8%)	0.256 (+1.6%)
2.5	0.313 (−69%)	0.0108 (−70%)	0.207 (−18%)
3.5	0.234 (−77%)	0.0158 (+56%)	0.219 (−13%)

$$\begin{aligned} \overline{C_{D,\mathrm{Bare}}} &= 0.722, \\ \hat{C}_{L,\mathrm{Bare}} &= 0.0325, \\ \overline{C_{S,\mathrm{Bare}}} &= 0.217. \end{aligned} \tag{6}$$

B. Vortex dynamics

It is known that as the wake width diminishes, a lower drag is imposed on the structure, because a lower pressure difference occurs between frontal and rear regions. The tendency of decay in $\overline{C_D}$ seen in Fig. 8 may be justified as so. This is pointed out by the vorticity contours of Fig. 9 (Multimedia view) for the cross-section at $z/L = 0$ (see Fig. 5 for the set of axes). The figure shows that the wake expanded with the insertion of passive rods compared with the bare cylinder [Fig. 9(a)], because the fixed rods simply established a larger obstruction to the flow. The wake sustained a similar aspect when the passive system ($\zeta = 0.0$) became just active ($\zeta = 0.5$). Nevertheless, from this

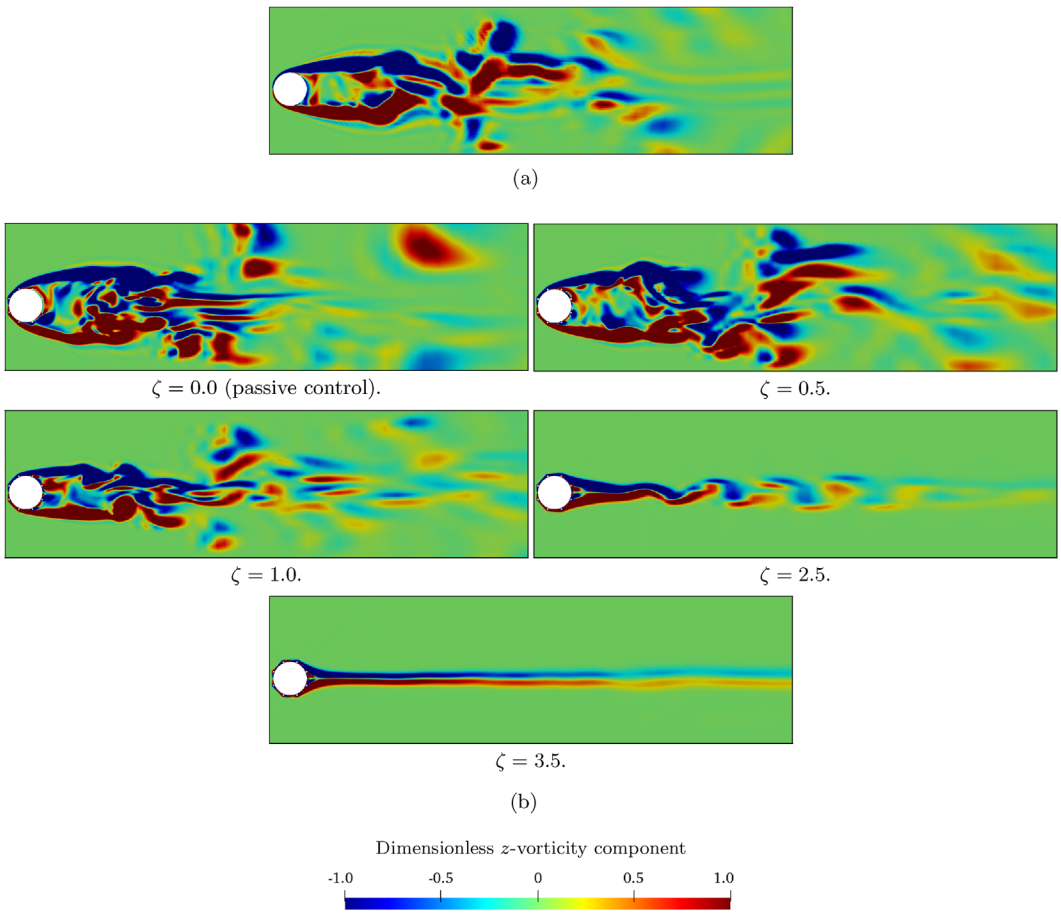

FIG. 9. Vorticity contours at $z/L = 0$ demonstrate the capacity of the active mechanism to attenuate vortex shedding and holistically eliminate the small vortices and turbulent eddies that dominate the wake for the bare cylinder and for the entire system at $\zeta = 0.0$ but that vanish from the flow domain at $\zeta = 3.5$. Instead, at the most active setup, occurred the formation, a very thin wake with rather residual emanation of vortices at a greater distance from the body. (a) Bare cylinder and (b) entire system. Multimedia view: https://doi.org/10.1063/5.0147760.1

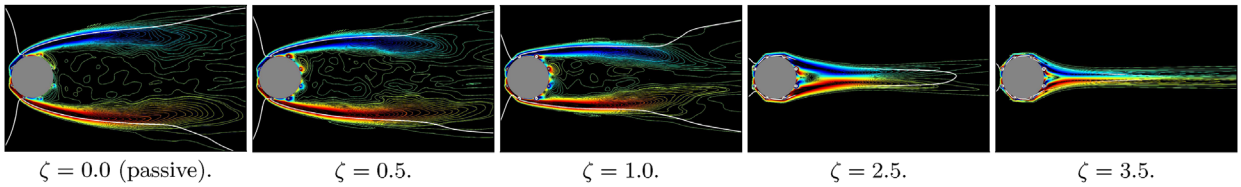

FIG. 10. Time-averaged vorticity contours exhibit progressive concentration of positive and negative vortices in a smaller region as the wake width shortened. This is followed by approaching shear layers (white line).

value of ζ onward, the spinning rods progressively reduced the wake width.

After the wake narrowed (see $\zeta \geq 1.0$ in Fig. 9) and the formation length shortened (as it is discussed below), an intensified interaction between Kármán vortices resulted thereof. Based on the mechanism of formation of vortices explained by Gerrard (1966), the closer the vortices were emanated longitudinally and transversely in the wake, the faster occurred the supply of vorticity from the shear layers to the vortices, their roll-up and shedding from one another. In terms of hydrodynamic loads, this translated into the appearance of the high frequency component of the hydrodynamic loads that is exposed in Fig. 8, particularly for the lift force, directly associated with the regions of low pressure formed interchangeably during their interaction. Vortex shedding was then attenuated and very small scales vanished from the flow domain as $\zeta = 2.5$ was reached. Figure 9 renders this clearer for $\zeta \geq 1.0$.

The reduction in wake width is better seen in Fig. 10 of the time-averaged vorticity contours at the cross section $z/L = 0$. The shear

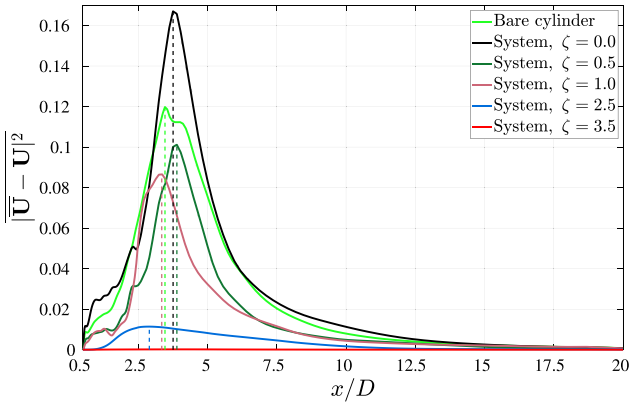

FIG. 11. Curves of $\overline{|\tilde{\mathbf{U}} - \mathbf{U}|^2}$ for the bare cylinder and for the entire system. At any level of rotation rates associated with ζ, the peaks were lower than in the bare cylinder case. In general, formation length (associated with the peak x-stations) decreased with higher rotation rates. At $\zeta = 2.5$, the peak was about 1/12 that of the bare cylinder. At $\zeta = 3.5$, the fluctuations were negligible.

layers are highlighted by a white line that corresponds to $0.99U_\infty$. The figure further exhibits that the negative (blue) and positive (red) oriented vorticity contours were confined in a small region past the system for the most active setups.

Figure 11 presents the time-averaged squared fluctuation of the velocity field that was taken along the x-direction in the plane $z/L = 0$. The formation length is highlighted by the dashed vertical lines at the coordinates of the maximum of each setup. We recall that the formation length is measured by the distance from the rear stagnation ($x = 0.5$) region to the point, downstream, where the velocity fluctuation reaches peak value (Williamson, 1996), decaying subsequently. The analysis above of the vorticity contours is corroborated by Fig. 11, which reveals that the insertion of fixed rods amounted to larger velocity fluctuation than that found for the bare cylinder. Contrastingly, the formation length shortened after $\zeta = 0.5$ up to 2.5, an apparently contradicting result when compared with Assi *et al.* (2019); Carvalho and Assi (2022), because as the formation length is prolonged, the viscosity tends to weaken the shear layers that subsequently roll up prior to becoming vortices. It is through this mechanism that splitter plates lead to wake control (Bearman, 1965). The same did not hold for the present active MSBC mechanism as far as shortening formation length is concerned. However, it must be acknowledged that the peaks of the different curves of $\overline{|\tilde{\mathbf{U}} - \mathbf{U}|^2}$ contracted with larger ζ. In fact, already at $\zeta = 0.5$, the system presented a lower peak than the bare cylinder and essentially zeroed in when $\zeta = 3.5$.

Contours of $|\tilde{\mathbf{U}} - \mathbf{U}|^2$ of Fig. 12 show that the fluctuations of the flow were cast away, provided the rods spun sufficiently fast and confirm that the passive control led to a larger region of velocity fluctuations (associated with the appearance of turbulent eddies), detected in Carvalho and Assi (2023c). Compared with the vorticity contours of this former work, the disappearance of any red region demonstrates the effectiveness of imposing rotation to the rods, but calls attention to the power expenditure. This topic is discussed in Sec. IV E.

In addition to the aforementioned features, given sufficient angular velocities, the matters of correlation and end effects stood out, as highlighted through Q-contours of vorticity magnitude in the spanwise y-view of Fig. 13 (Multimedia view).

Individually, the wake of the bare cylinder and of the less active setups was comprised of smaller structures near the bodies with greater vorticity content and larger eddies away that traveled throughout the three-dimensional flow domain. As the rods spun faster, the turbulent structures were progressively eliminated, and streamwise vortices became apparent, as depicted for $\zeta = 2.5$. In fact, it is easy to observe in Fig. 13 that in this arrangement, the otherwise correlated vortices were disrupted through the interaction with the tip-vortex of the finite bodies; hence, the well correlated structures observed in laminar and turbulent regimes for infinitely long structures of Carvalho *et al.* (2021) and Carvalho and Assi (2022), respectively, were not detected here.

It may be said that the rods acted on the bidimensional mechanism of vortex formation (Gerrard, 1966, also briefly reviewed in Sec. I) that one verifies to occur in an infinitely long cylinder (and systems with MSBC, Carvalho and Assi, 2022). When the end effects were entailed, instead, the rods were incapable of suppressing the tip-vortex, intrinsically related to a three-dimensional mechanism of vortex formation (Williamson, 1996).

Of course, two-dimensional (2D) contours in cross-sectional planes provide a simple visualization of the features of the rather 3D flow, fully represented in Fig. 14 (Multimedia view). It may be seen that for the bare cylinder much larger, but weaker structures, formed away from the body. For the system, this tendency was followed only for the passive mechanism and for $\zeta = 0.5$. At $\zeta = 1.0$, Q-contours exhibit a wake with fewer coherent structures near and away from the body, while for $\zeta = 2.5$ some correlation is visualized in eddies that emerge with a tube-like format, but that are affected by the tip-vortex. The resulting combination of these structures resemble "arch-vortices"

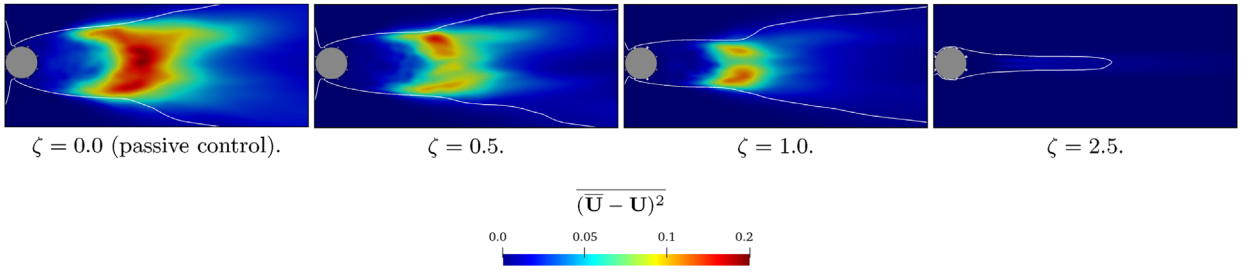

FIG. 12. Time-averaged contours of velocity fluctuation show that to insert fixed rods enlarged the region of high velocity fluctuation, but at any of the active regimes presently considered, this region was strongly weakened down to complete suppression ($\zeta = 2.5$).

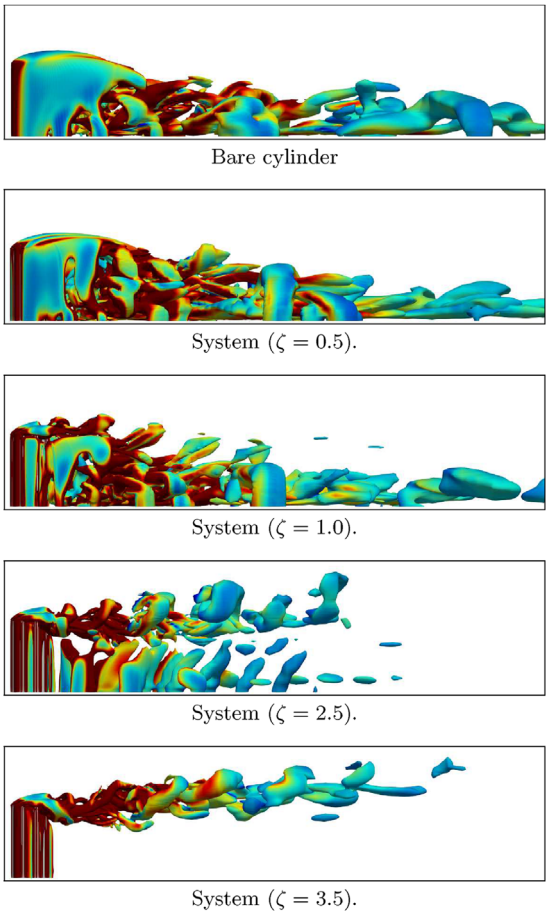

FIG. 13. *Q*-contours seen from a spanwise (*y*-) view. Streamwise vortices that were otherwise made perfectly correlated in laminar and turbulent regimes of infinitely long cylinders by the present system were acted upon by the tip-vortex. Even at $\zeta = 3.5$, tip-vortices remained in the wake with large vortical content. Multimedia view: https://doi.org/10.1063/5.0147760.2

(Taniguchi *et al.*, 1981). It is interesting to note that with this set of rotations, in turbulent infinitely long cases, vortex shedding occurred two-dimensionally, that is, vortices were perfectly correlated spanwise.

At $\zeta = 2.5$, *Q*-contours of high and low values (equal to 2.5, in red; and 0.1 in translucent blue) presented in Fig. 15 (Multimedia view) reveal that the rods were capable of suppressing the wake that originated along the spanwise extension of the cylinders through progressive weakening of the turbulent structures related to the Gerrard's (1966) mechanism of vortex generation in cylinders. This is made clear from the transition in colors. However, as the rods' spanned the passive mechanism toward the most active setups herein analyzed, the tip-vortices not only remained, but their vortical content was unaffected by the wake-control rods. This stands out in Fig. 15(b) ($\zeta = 2.5$): While most vortices were well correlated and with low vorticity (blue), ring-like red vortices (high vorticity) were produced on the free end.

Interestingly, it may be seen from the provided videos that as a result from the interaction of the tip-vortices with those streamwise-oriented, a flow structure reminiscent of the arch-vortices, previously observed in works of wall-mounted bodies, appeared (Sumner *et al.*, 2004). The videos discern, however, that these vortices did not form an arch *per se*, perhaps due to the momentum injected in the *z*-direction by the rods. This behavior differs from the experiments conducted by Sumner *et al.* (2004), where the authors showed that for $L/D < 3$, a symmetric "arch-vortex" dominated the near wake. The difference might lie in the boundary layer as well (as we used a free water surface, whereas there the cylinder was immersed into the boundary layer of the ground).

Clearly, as well, the present wake and the classical von Kármán wake are disparate, in agreement with experiments (Luo *et al.*, 1996; Sumner *et al.*, 2004) that did not detect the coherent wake for low slenderness parameter. Instead, while turbulent eddies lost vorticity by viscous dissipation, they were able to draw vorticity from smaller structures that were carried along. As these incorporated structures weakened and disappeared at the upper end of our ζ-range, tip-vortices approached more clearly a ring shape, particularly at $\zeta = 2.5$. As a matter of fact, for $\zeta = 3.5$, it is seen that streamwise vortices were eliminated from the wake and then only the tip-vortices remained.

In order to further assess end effects, components of the mean velocity field, project in the *y*–*z* plane, are shown in Fig. 16 for different *x*-stations. The first three positions correspond, respectively, to locations past the pair of cylinders P_1, P_1' ($x = -0.4$), P_2, P_2' ($x = 0.0$), and P_3, P_3' ($x = 0.4$); and the last two positions refer to planes that do not cross the system, but are located downstream (therefore past P_4, P_4').

The first column of Fig. 16 refers to the passive mechanism and exhibit the features detected in Carvalho and Assi (2023c). In a nutshell, this includes (1) the vectors representative of the flow from the free water surface (on the right of each figure) to the free end (on the left), (2) tip-vortex formation as the flow course is forced above, below and to the free end of the cylinders, and (3) the sustained vortices past the system, at $x/D = 1$. The other columns refer to the active mechanism ($\zeta = 0.5$, 1.0, 2.5, and 3.5).

Upstream of separation (at $x/D = -0.4$, first row of the figure), the velocity field shows that regardless of power input, the suppressing device did not affect the flow in the *y*–*z* plane substantially, which kept the overall aspect portrayed by Carvalho and Assi (2023c) for the finite bare cylinder under the effect of a free surface. Exception may regard only to some slight reduction in the magnitude of the velocity field distant from the side of the bodies (in the *z*-direction). For the other positions, there was a much more pronounced reduction in the velocity field away from the bodies. For example, it may be seen that, at $x/D = 0$, the flow from the free water surface to the tip of the bodies is gradually eliminated by the effect of the increasing velocities of the rods that might have redirected the flow to adopt the streamwise direction.

Although experimental data about the separation point of such a system are not available, it is reasonable to assume that at $x/D = 0.4$ (equivalent to $\theta > 156°$) separation had already taken place on the basis of (1) the angle of separation of a bare cylinder in the subcritical regime (according to Blevins, 1990, it is greater than 80° but less than 140°) for an infinitely long cylinder, (2) Farivar (1981) measured maximal pressure fluctuations at an angle of 75°, and (3) Figs. 9, 10, and 14 corroborate with this assumption even at the most active arrangements. At this position, we note that as the rods spun faster, the

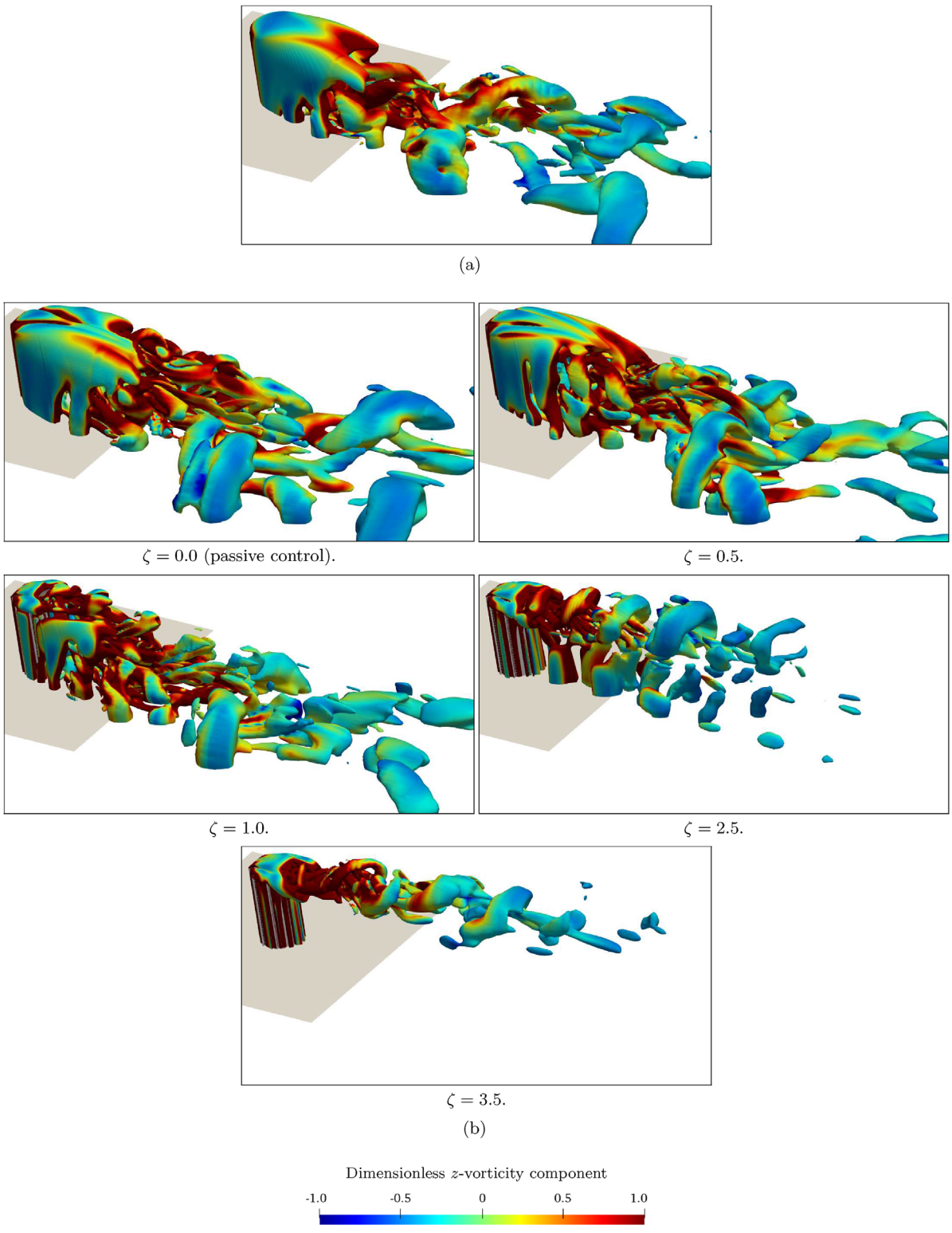

FIG. 14. Q-contours ($Q = 0.1$) present the three-dimensionality of the flow. Active rods suppressed most of the wake, but were unable to eliminate the tip-vortex. Red contours show that these vortices remained strong, even at $\zeta = 3.5$. (a) Bare cylinder and (b) entire system. Multimedia view: https://doi.org/10.1063/5.0147760.3

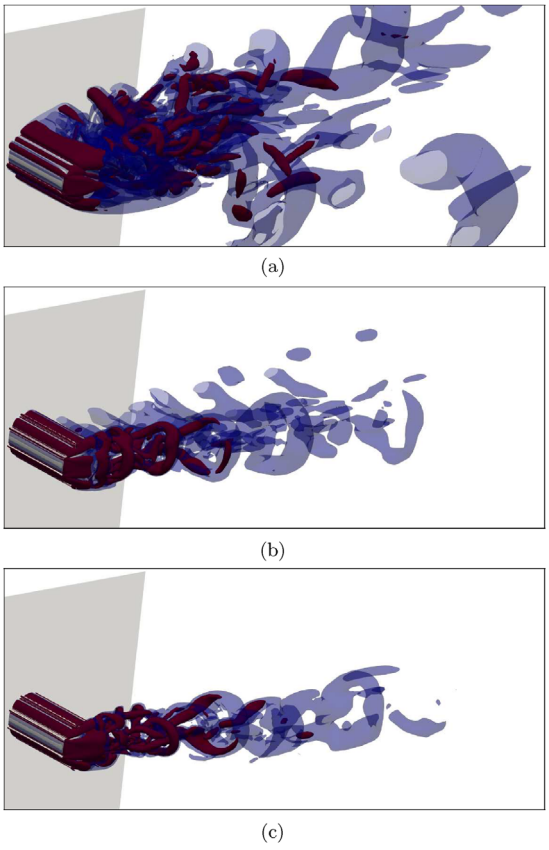

FIG. 15. High and low levels of Q contours corresponding to 2.5 (red) and 0.1 (blue, translucent). (a) Passive mechanism ($\zeta = 0.0$), (b) $\zeta = 2.5$, and (c) $\zeta = 3.5$. Multimedia view: https://doi.org/10.1063/5.0147760.4

orientation of the vectors reversed on the side of the bodies. Whereas in the passive mechanism the flow on the upper part adopted a counterclockwise sense (and the opposite for the lower part) at this position, this direction was gradually reversed. At $\zeta = 3.5$, the figure shows that the flow on the upper part swirled in a clockwise sense instead (and conversely for the lower rods). This means that the rods' spinning motion brought and induced the outer flow to follow the direction imposed by them. Although as a nuance, the same effect took place at $x/D = -0.4$, but there the upper rods P_1, P_1' merely forced the flow upward. This is seen by the rather vertical and parallel vectors along, but perpendicular to, the extension of the bodies. The difference between this effect at $x/D = -0.4$ and at $x/D = 0.4$ lies strictly on the location relative to the separation point.

The same underlying flow behavior was promoted by the rods for the x-stations located in the wake, those of $x = 0.6$ and $x = 1.0$: The flow surrounding the structure, which moved away from the free water surface (recall that the no-penetration condition applied), was pulled by the rods the more the faster they rotated (see these x-stations from left to right in Fig. 16). However, in these cases, a circulatory pattern was found at the fastest configurations, whereby upward and downward vectors represented in the figure mixed across $y = 0$. Yet, above and below $y = 0$, a circulatory pattern remained at $\zeta = 2.5$ and $\zeta = 3.5$ that corresponds to the formation of tip-vortices observed in Figs. 14 and 13, but much more clearly notable in Fig. 15, where the noteworthy ring-like vortex shape is noticeable. This projection of the tip-vortices in the y–z plane was combined and carried along downstream with the bulk of the flow in the x-direction to be later weakened by viscosity, prior to its utter elimination.

Since wake-control rods act in the sense of injecting momentum into the near flow of the entire system in a direction that is tangent to their cross section (in the x–y plane) to principally attenuate z-oriented vortices, it does not come as a surprise that this suppressing mechanism was not able to counteract the formation of tip-vortices, mostly aligned with the x-direction. Indeed, Fig. 8 demonstrates that the side force C_S, that is especially rooted in the tip-vortex, was marginally affected by the presence of the rods.

C. Hydrodynamic loads on the main body

We now quantitatively evaluate the hydrodynamic forces produced as a consequence of the vortex dynamics discussed above. Figure 17 throws some light on whether the insertion of the rods to the main body P_0 reduced mean drag, RMS of lift, and mean side force relative to the plain cylinder, through direct comparison between the loads upon P_0 and the reference values of Eq. (6) related to the bare cylinder.

It is easily seen that the wake-control rods brought significant reduction in the RMS of lift. Overall, the $\hat{C}_L$-curve shows a reduction greater than 23% ($\zeta = 0.5$). At best, we have verified a 75% decrease in $\hat{C}_L$ ($\zeta = 2.5$). At worst, rods' effect in $\hat{C}_L$ was a rather negligible uptick of 0.31% ($\zeta = 1.0$). For the mean drag, decrease was also noted at a less steeper tendency than $\hat{C}_L$, yet steady and monotonic with ζ. At $\zeta = 3.5$, the system was able to produce upon P_0 a mean drag 30% lower than that that affected the bare cylinder. Both the results in terms of $\hat{C}_L$ and $\overline{C_D}$ are directly related to the very essence of the MSBC mechanism: Momentum was transferred to the shear layers that caused their reattachment, as observed in Fig. 10. As a consequence, the thinner wake produced a smaller region of lower pressure past the system, and the difference in pressure fore and aft the system led to lower mean drag. Similarly, vortices were confined to interact in a shorter region, whereby they interacted more frequently. From Gerrard (1966), it is known that a vortex grows until another, opposite vortex, cuts off its vorticity supply. This happens more rapidly in a thin wake.

The same trend did not occur for $\overline{C_S}$, and the reason lies mainly on the mechanism of vortex formation. In lieu of the interaction of opposing vortices that is vital to form a Kármán street, or the present vortex wake of finite bodies shown above, these tip-vortices were rooted in the proneness of flow separation separation due to the geometry of the body. Note that there is a 90° angle between the length of the bodies (aligned with the z-direction) and their sides at the free end (aligned with the x-direction, at $z/L = 1$). The wake-control rods employed here could not affect $\overline{C_S}$ appreciably, as justified in Sec. IV B, but a light decrease in 5.5% was noted at $\zeta = 2.5$.

D. Hydrodynamic loads on each body

Mean force coefficients are represented in Fig. 18 for each rod. In general, it is seen that the mean drag on P_1, P_1' and P_2, P_2' went from positive to negative values, adopting then ever greater propulsion [a

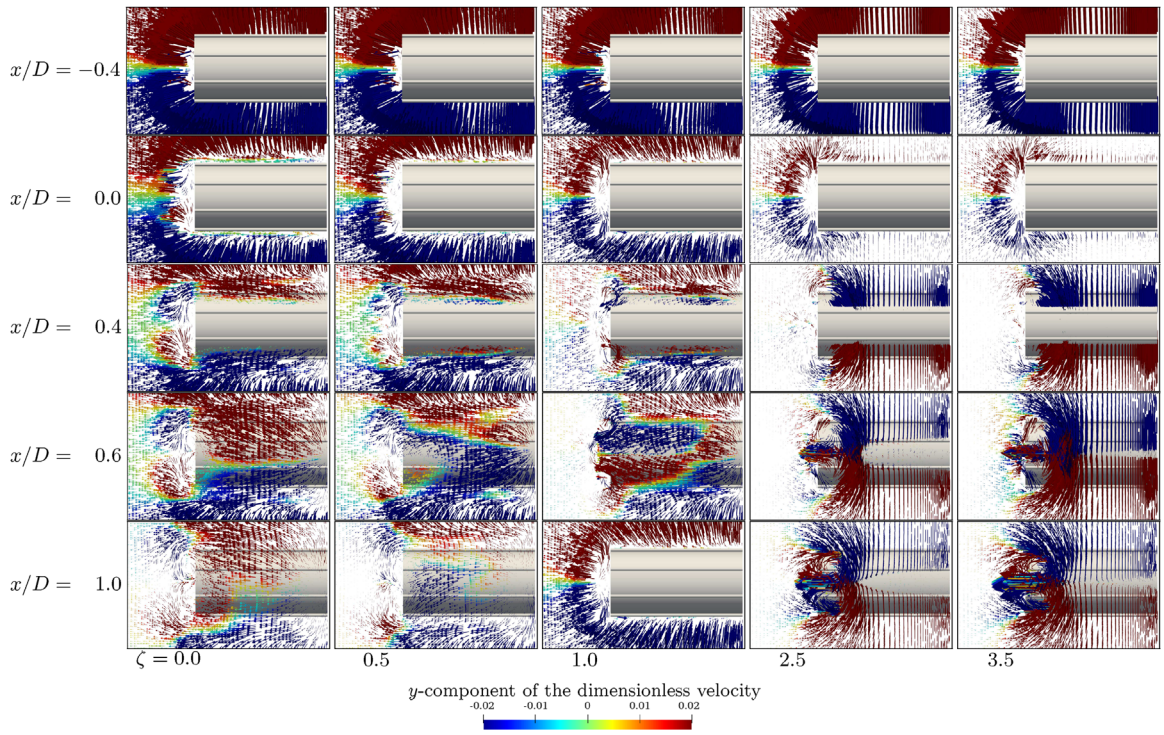

FIG. 16. Mean flow field over finite bodies projected in the *y*–*z* plane at different *x*-stations (lines) with increasingly faster rotation speeds (columns). The *z*-axis spans the length of the body from left to right of each subfigure. Blue and red correspond to upward and downward (in *y*) velocity vectors, respectively.

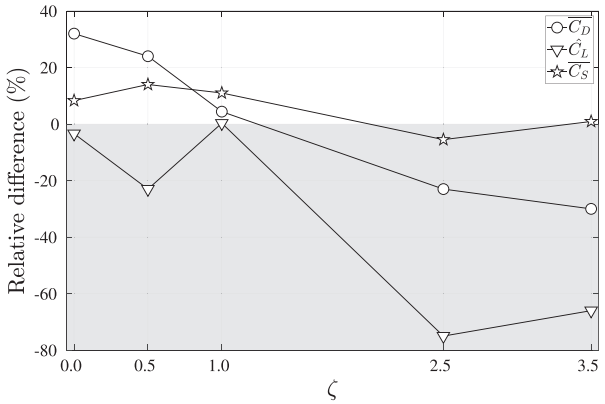

FIG. 17. Comparison between the RMS of lift ($\hat{C}_L$), mean drag ($\overline{C_D}$), and mean side force ($\overline{C_S}$) acting on the main body P_0 relative to the same loads found to act upon the bare cylinder. Shading corresponds to the region of attenuation of these loads.

horizontal force against the direction of the incoming flow, see Fig. 18(a)]. Contrarily, for P_3, P'_3 and P_4, P'_4, the loads generally passed from slightly negative and null values to positive and larger values. These monotonic tendencies seemed to prevail, particularly for the upper end of angular velocities hereby analyzed. The exception was the pair P_3, P'_3, because the loads went from essentially null (passive mechanism) to negative values ($\zeta = 1.0$) and then reversed to larger and positive mean drag ($\zeta = 2.5$ and $\zeta = 3.5$). These features are shared both by this plot and that of Carvalho and Assi (2022). The rods carrying most of the loads acting on the entire structure were the intermediate elements P_2, P'_2 and P_3, P'_3, more distant from stagnation regions, while P_1, P'_1 and P_4, P'_4, located in these regions, were less representative. As seen in the literature, intermediate rods can more easily interact with shear layers and affect separation points (Carvalho *et al.*, 2021; Carvalho and Assi, 2022; Carvalho and Assi, 2023c). This elucidates the far-reaching capacity of MSBC, capable of dealing even with the more complex flow structure of finite bluff bodies.

Difference between these setups lies essentially in the lower magnitudes of the mean loads for the finite bodies. On physical grounds, this difference is the outcome of the lower correlation found for turbulent flows about fully three-dimensional bodies, where end effects are present. In such cases, mean drag and mean lift tend to be lower, as flow modeling prevents information loss from the two-dimensional imposition of periodic boundary conditions on the ends.

In relation to mean lift, represented in Fig. 18(b), it is noted that all rods followed a monotonic tendency with greater angular velocities. The symmetry between positive lift applied on the upper rods and the negative lift on the lower rods led to mean null value of mean lift upon the entire structure and on the main body as in previous works for infinitely long bodies in laminar and turbulent regimes (Assi *et al.*, 2019; Carvalho *et al.*, 2021; and Carvalho and Assi, 2022).

Our data show that time-averaged drag, lift, and side force were comparable in the passive mechanism. However, when the rods were in motion, the $\overline{C_S}$ was broadly one order of magnitude below the other

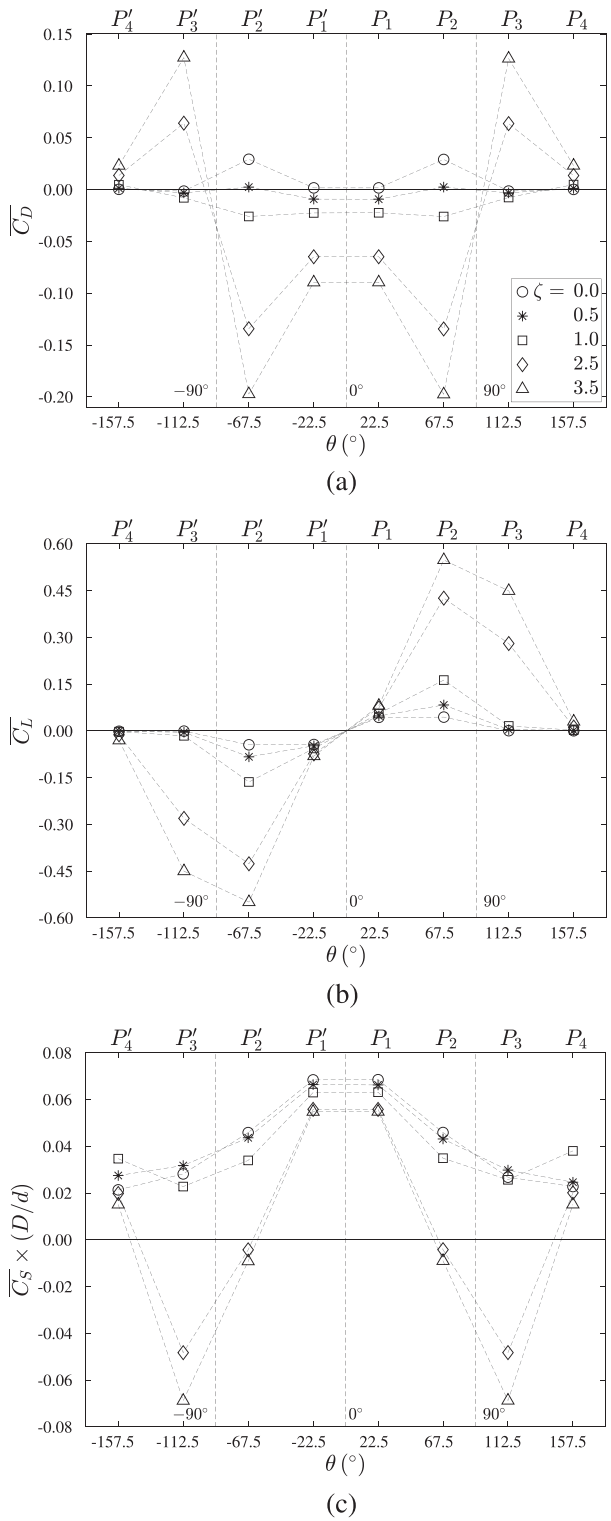

FIG. 18. Loads acting on each rod. (a) Mean drag, (b) mean lift, and (c) mean side force.

loads. For ease of interpretation, Fig. 18(c) represents the side force multiplied by $D/d = 20$. It is seen that the rods broke away from previous behaviors observed for $\overline{C_D}$ and $\hat{C}_L$: P_1 contributed significantly to the side force even at greater angular velocities and remained comparable to the most impacted rod, P_3, in these more power-demanding configurations. P_2 progressively became less relevant, and the same pattern was followed by P_4 (in common with the behavior detected for the other coefficients).

These observations point to the fact that with respect to $\overline{C_S}$, the position of the rods relative to the shear layers was not a key factor in determining their contributions. The $\overline{C_S}$-curves may be jointly analyzed in two groups: one for $\zeta \leq 1.0$ and the other for $\zeta \geq 2.5$, because the curves of these ranges near each other closely. Physically, this division permeates the degree of suppression of vortex shedding. For $\zeta \geq 2.5$ vorticity, contours of section B show that aside from the tip-vortex, the other flow structures in the wake were more strongly correlated than previous active setups, and at $\zeta = 3.5$, only the tip-vortex remained. Therefore, the influence of the rods on $\overline{C_S}$ was not related to the shear–layer interaction, but rather to the state of the wake and its imbalance in pressure along the span of the body. When the wake was not suppressed, a pressure difference along the span of the body amounted to greater $\overline{C_S}$.

This may be noted in Fig. 19, where it is shown that for the lower end of our range of ζ, the mean pressure coefficient gradually decreased toward lower values as it reached the interface between the system and the free stream. Contrarily, for the higher rotation rates, the $\overline{C_p}$ curve was generally flat at higher values until it abruptly lowered to the pressure at the interface. Note that (1) along the system, the values of $\overline{C_p}$ with $\zeta = 2.5$ and 3.5 were much greater than those for $\zeta \leq 1.0$, and these curves reached roughly the same value at the interface. From the high-pressure region (left, see $z/D = -1$) to the low-pressure region ($z/D = 1$), a force was generated in the z-positive direction for all curves. Now, (2) taking into account the free stream, the high pressure region is to the right ($z/D \to 6$ in the plot), asymptotically reaching $\overline{C_p} = 0$, a greater value than that at the interface, so a negative z-oriented force was produced from this pressure imbalance. These two forces summed to give the $\overline{C_S}$ higher for $\zeta \leq 1.0$ and lower otherwise. Further study is required to assess whether greater

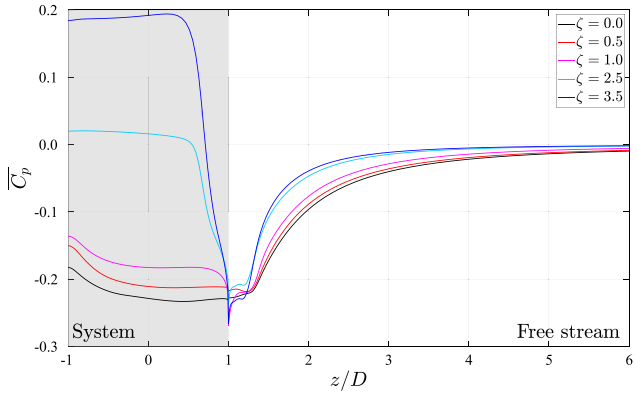

FIG. 19. Mean pressure coefficient along the z-direction, for $x/D = 0.5$ and $y/D = 0$. On the right is the free stream and on the left is the cylinder (shaded region). The interface lies at $z/D = 0$.

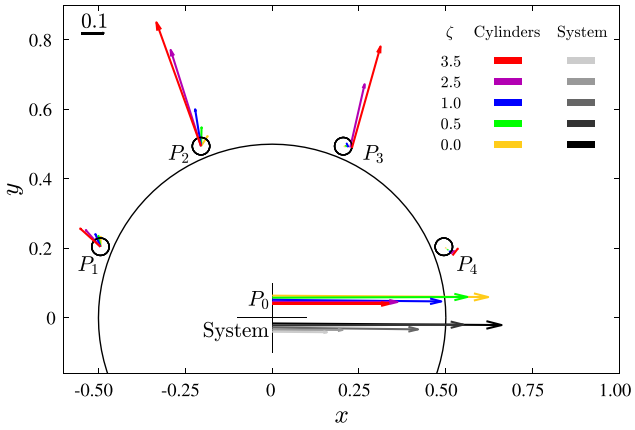

FIG. 20. Total force upon the rods shown by vectors. Groups of bars correspond to $\zeta = 0.0$, 0.5, 1.0, 2.5, and 3.5. Due to the symmetry of the setup in relation to the axial flow, rods P_n, P'_n, $n = 1, \ldots, 4$ were acted upon by the same load magnitudes and were omitted for the sake of conciseness.

angular speeds would be able to maintain this tendency of increase in $\overline{C_P}$ over the cylinder that could eventually eliminate $\overline{C_S}$.

Curiously, present results encompassing all the components of the resultant force on each rod emphasize by and large that P_4 may be less germane to the attenuation of hydrodynamic loads.

The resultant loads on each cylinder (colored) and on the entire system (grayscale) are portrayed qualitatively by Fig. 20 for the upper rods (due to symmetry, the loads on the lower rods are the same, but mirrored with respect to $y = 0$). Because, as explained above, $\overline{C_S}$ was at least an order of magnitude lower than the other loads, the effect of the mean force was relatively negligible in the composition of the total load; thus, we have opted to represent only the x–y plane. General tendencies observed for infinitely long bodies were detected in the loads upon finite bodies: A monotonic increase for all rods (as plotted in Fig. 21); greater relevance of P_2 and P_3, since they concentrated higher loads; inversion in the x-direction of the loads on P_1, P_2, and P_3, while that on P_4 followed a singular direction; consistent reduction in the load upon the entire system, and it was kept essentially aligned with the flow direction (as expected by symmetry). For comparison, these loads were lower than those in the infinitely long case, but still within the same order of magnitude.

E. Power expenditure

Flow control was improved as the rods were put in spinning motion. In order to do so, an actuating power was required. We follow the analysis of Shukla and Arakeri (2013) to assess the effectiveness of the present system. According to these authors, the power loss of the entire system (C_{PL}) may be decomposed into the power spent to counteract the wall shear stress (C_N) and to downsize mean drag (C_D). We employ mean quantities (marked with an overbar) in the following equation:

$$\overline{C_{PL}} = \overline{C_D} + \overline{C_N}, \tag{7}$$

where time-averaging was performed as described in Sec. V. The mean wall shear stress $\overline{\tau_n}$ was integrated over the entire surface of the bodies ($\overline{p_n}$). The first part of the right hand side of the following equation refers to integration over the span, while the second is on the sides of the rods:

$$\overline{p_n} = \omega_n \frac{d}{2}\left\{\int_{-L/2}^{L/2}\left[\int_0^{2\pi}\overline{\tau_n}\,\frac{d}{2}\,\mathrm{d}\theta\right]\mathrm{d}z + \int_0^{D/2}\left[\int_0^{2\pi}\overline{\tau_n}\,r\mathrm{d}\theta\right]\mathrm{d}r\right\}. \tag{8}$$

Normalization is made to get $\overline{C_N}$ is given in the following equation:

$$\overline{C_N} = \sum_{n=1}^{N}\frac{\overline{p_n}}{\frac{1}{2}\rho U_\infty^3 DL}. \tag{9}$$

The curve $\overline{C_D}$ vs $\overline{C_N}$ plotted in Fig. 22 allows to assert that the mean drag upon the entire system was predominant in the components of $\overline{C_{PL}}$ up to $\zeta = 1.0$. The situation reversed for $\zeta \geq 2.5$. This can be viewed from markers to the left and to the right, respectively, of the dashed line plotted after $\overline{C_D} = \overline{C_N}$ in the same figure. Therefore, the presented trend suggests that depending on the amount of power provided to the system, it may occur a situation such that a greater fraction of the actuating power is spent to spin the rods rather than to

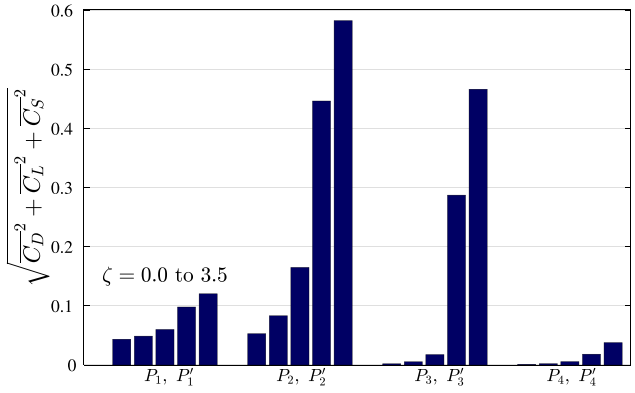

FIG. 21. Bars represent the total force upon the rods. Groups of bars correspond to $\zeta = 0.0$, 0.5, 1.0, 2.5, and 3.5. Due to the symmetry of the setup in relation to the axial flow, rods P_n, P'_n, $n = 1, \ldots, 4$ were acted upon by the same load magnitudes.

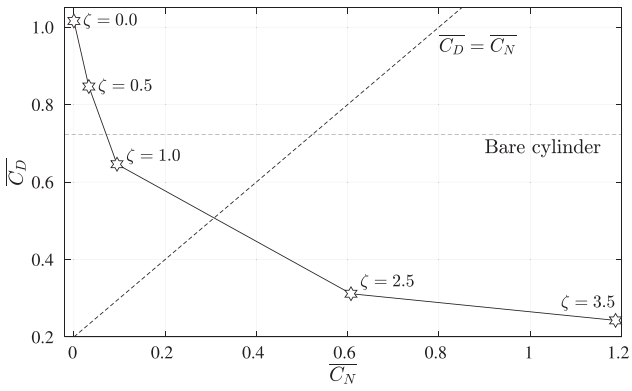

FIG. 22. Time-averaged components of the mean power loss, the mean drag upon the entire system $\overline{C_D}$, and the power-loss due to viscous friction $\overline{C_N}$. Right and left of the dashed line $\overline{C_D} = \overline{C_N}$ indicate two regions, respectively, one where $\overline{C_D}$ and another where $\overline{C_N}$ dominates.

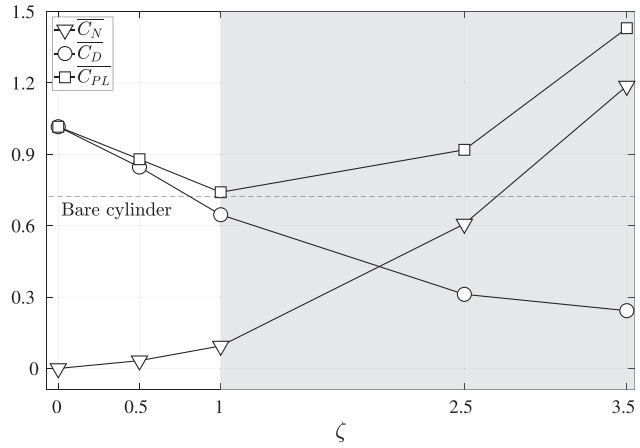

FIG. 23. Mean power-loss coefficient $\overline{C_{PL}}$ and its components $\overline{C_N}$ and $\overline{C_D}$ over the entire system. In the shaded region, $\overline{C_D} < \overline{C_{D,\text{Bare}}}$.

improve flow control (here in the scope of $\overline{C_D}$ attenuation and vortex shedding suppression). These circumstances were not evaluated here, but may be thought of, for example, given $\zeta \geq 3.5$. Vorticity contours shown earlier suggest that wake suppression was maximal in such angular speeds arrangement, and as discussed, one might not expect the rods to eliminate the tip-vortex. Therefore, it seems likely that $\zeta > 3.5$ would correspond to a state of the flow where more power input would not leverage flow control over the tip-vortex, but it may be possible that the system would be submitted to a turnaround where $\overline{C_D} < 0$, as in previous works (Silva-Ortega and Assi, 2017b; Assi *et al.*, 2019; and Carvalho and Assi, 2022).

Equation (7) provides a way to assess the efficiency of the entire system with the computed power-loss coefficient $\overline{C_{PL}}$ plotted in Fig. 23.

The figure outlines that in order to reduce the mean drag over the present system below $\overline{C_{D,\text{Bare}}}$, as it occurred for $\zeta \geq 1.0$, power expenditure is key, since $\overline{C_{PL}} \gtrapprox \overline{C_{D,\text{Bare}}}$. Furthermore, the figure depicts that a steep rise occurred in $\overline{C_N}$, which became the major part of $\overline{C_{PL}}$ already at $\zeta = 2.5$. Indeed, to use this active mechanism for a finite system required more power to counteract viscous traction than for infinitely long bodies. This trade-off between power expenditure and drag reduction establishes an optimization problem that requires further study for a system as the present in the same fashion as those conducted for simpler arrangements, with fewer slender rods (Fan *et al.*, 2020; Bingham *et al.*, 2018).

V. CONCLUSION

Vortex dynamics, hydrodynamic loads, and power efficiency were numerically investigated with respect to finite bodies through Detached-eddy simulations (DES). A bare cylinder (one without flow control device) and a system (as in Silva-Ortega and Assi, 2017b), comprised of this body and eight slender wake-control rods, were analyzed in the turbulent regime at Reynolds number of 1000. Upper and lower rods spun symmetrically, with angular velocities obtained from potential flow about a bare cylinder (Carvalho *et al.*, 2021). The rods rotated faster through the parameter $\zeta = 0.0$ (passive mechanism), 0.5, 1.0, 2.5, and 3.5 that multiplied the velocities. A free water surface, modeled here as a slip-allowing plane, was attached to one end of the cylinders.

Vorticity contours showed that to fit the main body with spinning rods was capable of eliminating the wake originated by a "two-dimensional" mechanism of wake formation (Gerrard, 1966) that consists on vortices produced by separation of the boundary layer as the fluid flows about the bluff body. In order to achieve so, sufficiently large actuating power was given to the system. Nevertheless, separation from the ends of the bodies generated tip-vortices (Kawamura *et al.*, 1984) upon which the active mechanism had little effect and that remained with strong vortical content even at suppression of the other eddies. Spanwise visualization of Q-contours showed that finite bodies' wakes broke away from the perfectly correlated vortex shedding pattern previously found for infinitely long bodies (with large enough angular velocities Carvalho and Assi, 2022).

Flow control released by the active rods with progressively larger angular velocities was accompanied by the contraction of the wake, elimination of mean velocity fluctuations, and reduction of vorticity content within the eddies. Velocity vector field presented for cross sections passing through different streamwise positions revealed that the energy provided to rods' revolutions was translated into momentum injection to a point that the outer flow was induced to adopt the streamwise direction. Furthermore, the recirculation direction was reversed from passive to active mechanism, with threshold detected at $\zeta = 2.5$. This interference with the flow caused the formation of novel ring-like vortices that lasted throughout our range of ζ. At the onset of their formation, these vortices drew smaller vortices, in such a fashion that compensated vorticity loss due to viscosity nearer to the system.

In terms of hydrodynamic loads, addition of the rods led to significant and steady attenuation of mean drag, and light reduction of the root mean square (RMS) of lift and mean side force. These two latter forces were mitigated only more sensibly for $\zeta \geq 2.5$ and 3.5, although these two arrangements differed but marginally. Comparison with the bare cylinder showed that mean drag and RMS of lift reduced by up to 23% and 75%, while the mean side force was negligibly affected.

Efficiency of the entire system analyzed on the basis of power-loss coefficient (Shukla and Arakeri, 2013) rendered clear that in order to mitigate mean drag, power expenditure was key to counteract wall shear stress due to viscous effects. Our analysis also corroborated with previous studies in that this source of power-loss became dominant as the rods spun faster. Power-loss coefficient was 27% and 98% above that of the bare cylinder to reduce the mean drag in 57% and 66%, respectively.

Finally, we remark that to the best of our knowledge, the literature on flow control of finite bodies is scarce, and the present analysis with wake-control rods was not conducted previously. Active control of the wake of stationary bluff bodies is a stepping stone toward more complex configurations, such as that involving vortex-induced vibrations (VIV) of these structures, rooted in the vortex shedding mechanism. Future work should concern with the optimization of the angular velocities ω_n toward drag mitigation, production of a useful hydrodynamic load to maneuver the body or with the system free to oscillate in VIV.

ACKNOWLEDGMENTS

I.A.C. is grateful to CAPES Brazilian Ministry of Education for his Ph.D. scholarship and to the National Laboratory for Scientific

Computing (LNCC/MCTI, Brazil) for providing HPC resources of the SDumont supercomputer. GRSA acknowledges the support of FAPESP, Brazil (No. 2011/00205-6) and CNPq, Brazil (No. 306146/2019-3). We gratefully acknowledge the support of the RCGI Research Centre for Greenhouse Gas Innovation, hosted by the University of São Paulo, Brazil and sponsored by FAPESP (No. 2020/15230-5) and Shell Brazil.

AUTHOR DECLARATIONS

Conflict of Interest

The authors have no conflicts to disclose.

Author Contributions

Icaro Amorim Carvalho: Conceptualization (equal); Formal analysis (equal); Investigation (equal); Methodology (equal); Software (equal); Supervision (equal); Validation (equal); Visualization (equal); Writing – original draft (equal); Writing – review & editing (equal). **Gustavo R. S. Assi:** Conceptualization (equal); Formal analysis (equal); Funding acquisition (equal); Methodology (equal); Resources (equal); Software (equal); Supervision (equal); Visualization (equal); Writing – review & editing (equal).

DATA AVAILABILITY

The data that support the findings of this study are available from the corresponding author upon reasonable request.

REFERENCES

Assi, G. R., Bearman, P. W., and Kitney, N., "Low drag solutions for suppressing vortex-induced vibration of circular cylinders," J. Fluids Struct. **25**, 666–675 (2009).

Assi, G. R., Bearman, P. W., and Tognarelli, M. A., "On the stability of a free-to-rotate short-tail fairing and a splitter plate as suppressors of vortex-induced vibration," Ocean Eng. **92**, 234–244 (2014).

Assi, G. R. S., Orselli, R. M., and Silva-Ortega, M., "Control of vortex shedding from a circular cylinder surrounded by eight rotating wake-control cylinders at Re= 100," J. Fluids Struct. **89**, 13–24 (2019).

Bearman, P., "Investigation of the flow behind a two-dimensional model with a blunt trailing edge and fitted with splitter plates," J. Fluid Mech. **21**, 241–255 (1965).

Behr, M., Hastreiter, D., Mittal, S., and Tezduyar, T., "Incompressible flow past a circular cylinder: Dependence of the computed flow field on the location of the lateral boundaries," Comput. Methods Appl. Mech. Eng. **123**, 309–316 (1995).

Behr, M., Liou, J., Shih, R., and Tezduyar, T., "Vorticity-streamfunction formulation of unsteady incompressible flow past a cylinder: Sensitivity of the computed flow field to the location of the outflow boundary," Int. J. Numer. Methods Fluids **12**, 323–342 (1991).

Bingham, C., Raibaudo, C., Morton, C., and Martinuzzi, R., "Suppression of fluctuating lift on a cylinder via evolutionary algorithms: Control with interfering small cylinder," Phys. Fluids **30**, 127104 (2018).

Blevins, R. D., *Flow-Induced Vibration*, 2nd ed. (Van Nostrand Reinhold, New York, 1990).

Carvalho, I. A. and Assi, G. R. S., "Enhanced control of the turbulent flow past a circular cylinder with rotating rods inspired by an inviscid solution," J. Fluids Struct. **113**, 103652 (2022).

Carvalho, I. A. and Assi, G. R. S., "On the omnidirectionality of a system with eight spinning rods for wake control," J. Fluid Mech. (unpublished).

Carvalho, I. A. and Assi, G. R. S., "On the omnidirectionality of a system with eight spinning rods in controlling the wake of a circular cylinder in a turbulent regime," J. Fluid Mech. (unpublished).

Carvalho, I. A. and Assi, G. R. S., "Passive control of vortex-shedding past finite cylinders under the effect of a free surface," Phys. Fluids **35**, 015109 (2023c).

Carvalho, I. A., Assi, G. R. S., and Orselli, R. M., "Wake control of a circular cylinder with rotating rods: Numerical simulations for inviscid and viscous flows," J. Fluids Struct. **106**, 103385 (2021).

Choi, H., Jeon, W.-P., and Kim, J., "Control of flow over a bluff body," Annu. Rev. Fluid Mech. **40**, 113–139 (2008).

Cicolin, M. M. and Assi, G. R. S., "Experiments with flexible shrouds to reduce the vortex-induced vibration of a cylinder with low mass and damping," Appl. Ocean Res. **65**, 290–301 (2017).

Fan, D., Yang, L., Wang, Z., Triantafyllou, M. S., and Karniadakis, G. E., "Reinforcement learning for bluff body active flow control in experiments and simulations," Proc. Natl. Acad. Sci. U. S. A. **117**, 26091–26098 (2020).

Farivar, D., "Turbulent uniform flow around cylinders of finite length," AIAA J. **19**, 275–281 (1981).

Ferziger, J. H., Perić, M., and Street, R. L., *Computational Methods for Fluid Dynamics* (Springer, 2002), Vol. 3.

Fujarra, A. L., Rosetti, G. F., de Wilde, J., and Gonçalves, R. T., "State-of-art on vortex-induced motion: A comprehensive survey after more than one decade of experimental investigation," in *International Conference on Offshore Mechanics and Arctic Engineering* (American Society of Mechanical Engineers, 2012), Vol. 44915, pp. 561–582.

Gerrard, J. H., "The mechanics of the formation region of vortices behind bluff bodies," J. Fluid Mech. **25**, 401–413 (1966).

Gonçalves, R., Franzini, G., Rosetti, G. F., Meneghini, J., and Fujarra, A., "Flow around circular cylinders with very low aspect ratio," J. Fluids Struct. **54**, 122–141 (2015).

Gonçalves, R. T., Fujarra, A. L., Rosetti, G. F., and Nishimoto, K., "Mitigation of vortex-induced motion (VIM) on a monocolumn platform: Forces and movements," J. Offshore Mech. Arct. Eng. **132**, 041102 (2010).

Gonçalves, R. T., Meneghini, J. R., and Fujarra, A. L., "Vortex-induced vibration of floating circular cylinders with very low aspect ratio," Ocean Eng. **154**, 234–251 (2018).

Goodarzi, M. and Dehkordi, E. K., "Geometrical parameter analysis on stabilizing the flow regime over a circular cylinder using two small rotating controllers," Comput. Fluids **145**, 129–140 (2017).

Kawamura, T., Hiwada, M., Hibino, T., Mabuchi, I., and Kumada, M., "Flow around a finite circular cylinder on a flat plate: Cylinder height greater than turbulent boundary layer thickness," Bull. JSME **27**, 2142–2151 (1984).

Kim, S.-E., and Mohan, L. S., "Prediction of unsteady loading on a circular cylinder in high Reynolds number flows using large eddy simulation," in International Conference on Offshore Mechanics and Arctic Engineering (2005), Vol. 41979, pp. 775–783.

Korkischko, I. and Meneghini, J. R., "Volumetric reconstruction of the mean flow around circular cylinders fitted with strakes," Exp. Fluids **51**, 1109–1122 (2011).

Luo, S., Gan, T., and Chew, Y., "Uniform flow past one (or two in tandem) finite length circular cylinder (s)," J. Wind Eng. Ind. Aerodyn. **59**, 69–93 (1996).

Mittal, S., "Control of flow past bluff bodies using rotating control cylinders," J. Fluids Struct. **15**, 291–326 (2001).

Mittal, S. and Kumar, B., "Flow past a rotating cylinder," J. Fluid Mech. **476**, 303–334 (2003).

Newman, J. N., *Marine Hydrodynamics* (The MIT Press, 2018).

Norberg, C., "Flow around a circular cylinder: Aspects of fluctuating lift," J. Fluids Struct. **15**, 459–469 (2001).

Palau-Salvador, G., Stoesser, T., Fröhlich, J., Kappler, M., and Rodi, W., "Large eddy simulations and experiments of flow around finite-height cylinders," Flow, Turbul. Combust. **84**, 239–275 (2010).

Patankar, S. V., *Numerical Heat Transfer and Fluid Flow* (Taylor & Francis, 1980).

Rhie, C. and Chow, W. L., "Numerical study of the turbulent flow past an airfoil with trailing edge separation," AIAA J. **21**, 1525–1532 (1983).

Rosetti, G. F., Vaz, G., Hoekstra, M., Gonçalves, R. T., and Fujarra, A. L., "CFD calculations for free-surface-piercing low aspect ratio circular cylinder with solution verification and comparison with experiments," in *International Conference on Offshore Mechanics and Arctic Engineering* (American Society of Mechanical Engineers, 2013), Vol. 55416.

Shukla, R. K. and Arakeri, J. H., "Minimum power consumption for drag reduction on a circular cylinder by tangential surface motion," J. Fluid Mech. **715**, 597–641 (2013).
Silva-Ortega, M. and Assi, G. R. S., "Flow-induced vibration of a circular cylinder surrounded by two, four and eight wake-control cylinders," Exp. Therm. Fluid Sci. **85**, 354–362 (2017a).
Silva-Ortega, M. and Assi, G., "Suppression of the vortex-induced vibration of a circular cylinder surrounded by eight rotating wake-control cylinders," J. Fluids Struct. **74**, 401–412 (2017b).
Silva-Ortega, M. and Assi, G., "Hydrodynamic loads on a circular cylinder surrounded by two, four and eight wake-control cylinders," Ocean Eng. **153**, 345–352 (2018).
Smagorinsky, J., "General circulation experiments with the primitive equations: I. The basic experiment," Mon. Weather Rev. **91**, 99–164 (1963).
Spalart, P., "Trends in turbulence treatments," in Fluids 2000 Conference and Exhibit, 2000.
Spalart, P. R., "Comments on the feasibility of LES for wings, and on a hybrid RANS/LES approach," in *Proceedings of the First AFOSR International Conference on DNS/LES* (Greyden Press, 1997).
Spalart, P. and Allmaras, S., "A one-equation turbulence model for aerodynamic flows," in 30th Aerospace Sciences Meeting and Exhibit, 1992.
Spalart, P. R., Deck, S., Shur, M. L., Squires, K. D., Strelets, M. K., and Travin, A., "A new version of detached-eddy simulation, resistant to ambiguous grid densities," Theor. Comput. Fluid Dyn. **20**, 181–195 (2006).
Strykowski, P. J. and Sreenivasan, K. R., "On the formation and suppression of vortex shedding at low Reynolds numbers," J. Fluid Mech. **218**, 71–107 (1990).
Sumner, D., "Flow above the free end of a surface-mounted finite-height circular cylinder: A review," J. Fluids Struct. **43**, 41–63 (2013).
Sumner, D., Heseltine, J., and Dansereau, O., "Wake structure of a finite circular cylinder of small aspect ratio," Exp. Fluids **37**, 720–730 (2004).
Taniguchi, S., Sakamoto, H., and Arie, M., "Flow around circular cylinders of finite height placed vertically in turbulent boundary layers," Bull. JSME **24**, 37–44 (1981).
Tennekes, H. and Lumley, J. L., *A First Course in Turbulence* (MIT Press, 1972).
Travin, A., Shur, M., Strelets, M., and Spalart, P., "Detached-eddy simulations past a circular cylinder," Flow, Turbul. Combust. **63**, 293–313 (2000).
Vatsa, V. N., Lockard, D. P., and Spalart, P. R., "Grid sensitivity of SA-based Delayed-Detached-Eddy-Simulation model for blunt-body flows," AIAA J. **55**, 2842–2847 (2017).
Versteeg, H. K. and Malalasekera, W., *An Introduction to Computational Fluid Dynamics: The Finite Volume Method* (Pearson Education, 2007).
Williamson, C. H. K., "Vortex dynamics in the cylinder wake," Annu. Rev. Fluid Mech. **28**, 477–539 (1996).
Williamson, C. H. K. and Govardhan, R., "Vortex-induced vibrations," Annu. Rev. Fluid Mech. **36**, 413–455 (2004).
Zdravkovich, M. M., "Review and classification of various aerodynamic and hydrodynamic means for suppressing vortex shedding," J. Wind Eng. Ind. Aerodyn. **7**, 145–189 (1981).

Physics of Fluids

ERRATUM | JUNE 13 2023

Erratum: "Active control of vortex shedding past finite cylinders under the effect of a free surface" [Phys. Fluids 35, 045130 (2023)]

I. A. Carvalho ; G. R. S. Assi

Physics of Fluids 35, 069901 (2023)
https://doi.org/10.1063/5.0159286

Physics of Fluids ERRATUM pubs.aip.org/aip/pof

Erratum: "Active control of vortex shedding past finite cylinders under the effect of a free surface" [Phys. Fluids 35, 045130 (2023)]

Cite as: Phys. Fluids **35**, 069901 (2023); doi: 10.1063/5.0159286
Submitted: 22 May 2023 · Accepted: 1 June 2023 ·
Published Online: 13 June 2023

I. A. Carvalho[1,a] and G. R. S. Assi[2,b]

AFFILIATIONS

[1]Department of Mechanical Engineering, EPUSP, University of São Paulo, SP 05508-030, Brazil
[2]Department of Naval Architecture and Ocean Engineering, EPUSP, University of São Paulo, SP 05508-030, Brazil

[a]Author to whom correspondence should be addressed: amorim.icaro@usp.br
[b]Electronic mail: g.assi@usp.br

https://doi.org/10.1063/5.0159286

In Carvalho and Assi (2023), "We used $d/D = 0.1$" should be "We used $d/D = 0.05$."

Carvalho, I. A. and Assi, G. R. S., "Active control of vortex shedding past finite cylinders under the effect of a free surface," Phys. Fluids **35**, 045130 (2023).